Stable water isotope signals and their relation to stratiform and convective precipitation in the tropical Andes

Nadja Landshuter[1], Franziska Aemisegger[2], and Thomas Mölg[1]

[1]Friedrich-Alexander-University Erlangen-Nürnberg
[2]ETH Zürich

January 16, 2024

Abstract

Stratiform and convective precipitation are known to be associated with distinct isotopic fingerprints in the tropics. Such rain type specific isotope signals are of key importance for climate proxies based on stable isotopes like for example ice cores and tree rings and can be used for climate reconstructions of convective activity. However, recently, the relation between rain type and isotope signal has been intensively discussed. While some studies point out the importance of deep convection for strongly depleted isotope signals in precipitation, other studies emphasize the role of stratiform precipitation for low concentrations of the heavy water isotopes. Uncertainties arise from observational studies as they mainly consider oceanic regions and mostly long aggregation timescales, while modelling approaches with global climate models cannot explicitly resolve convective processes and rely on parametrization. As high-resolution climate models are particularly important for studies over complex topography, we applied the isotope-enabled version of the high-resolution climate model from the Consortium for Small-Scale Modelling (COSMOiso) over the Andes of tropical south Ecuador, South America, to investigate the influence of stratiform and convective rain on the stable oxygen isotope signal of precipitation (δ18OP). Our results highlight the importance of deep convection for depleting the isotopic signal of precipitation and increasing the secondary isotope variable deuterium excess. Moreover, we found that an opposing effect of shallow and deep convection on the δ18OP signal. Based on these results, we introduce a shallow and deep convective fraction to analyze the effect of rain types on δ18OP.

Hosted file

982471_0_art_file_11729610_s6dmqh.docx available at https://authorea.com/users/713242/articles/697594-stable-water-isotope-signals-and-their-relation-to-stratiform-and-convective-precipitation-in-the-tropical-andes

Stable water isotope signals and their relation to stratiform and convective precipitation in the tropical Andes

Nadja Landshuter[1] , Franziska Aemisegger[2] and Thomas Mölg[1]

[1]Climate System Research Group, Institute of Geography, Friedrich-Alexander-Universität Erlangen-Nürnberg, Erlangen, Germany.

[2]Institute for Atmospheric and Climate Science, ETH Zurich, Zurich, Switzerland

Corresponding author: Nadja Landshuter (nadja.landshuter@fau.de)

Key Points:

- Different rain types (stratiform, shallow and deep convection) are associated with distinct $\delta^{18}O_P$ and deuterium excess signals.
- Deep convection leads to the lowest $\delta^{18}O_P$ and the highest deuterium excess.
- A deep convective fraction or shallow convective fraction for correlations with $\delta^{18}O_P$ robustly capture the relation to rain types.

Abstract

Stratiform and convective precipitation are known to be associated with distinct isotopic fingerprints in the tropics. Such rain type specific isotope signals are of key importance for climate proxies based on stable isotopes like for example ice cores and tree rings and can be used for climate reconstructions of convective activity. However, recently, the relation between rain type and isotope signal has been intensively discussed. While some studies point out the importance of deep convection for strongly depleted isotope signals in precipitation, other studies emphasize the role of stratiform precipitation for low concentrations of the heavy water isotopes. Uncertainties arise from observational studies as they mainly consider oceanic regions and mostly long aggregation timescales, while modelling approaches with global climate models cannot explicitly resolve convective processes and rely on parametrization. As high-resolution climate models are particularly important for studies over complex topography, we applied the isotope-enabled version of the high-resolution climate model from the Consortium for Small-Scale Modelling ($COSMO_{iso}$) over the Andes of tropical south Ecuador, South America, to investigate the influence of stratiform and convective rain on the stable oxygen isotope signal of precipitation ($\delta^{18}O_P$). Our results highlight the importance of deep convection for depleting the isotopic signal of precipitation and increasing the secondary isotope variable deuterium excess. Moreover, we found that an opposing effect of shallow and deep convection on the $\delta^{18}O_P$ signal. Based on these results, we introduce a shallow and deep convective fraction to analyze the effect of rain types on $\delta^{18}O_P$.

Plain Language Summary

Tropical rainfall can be classified as convective and stratiform rain, which carry fingerprints in their water isotope signal. This implies that climate reconstructions of convective activity can be made, because the isotopic signal in precipitation is conserved in climate archives like ice cores or tree rings. Contrasting results emerged from observations, due to data scarcity, and from global climate models, which have shortcomings due to coarse spatial and temporal resolutions. We addressed the question of the influence of different rain types on the isotopic signal of precipitation by using a high-resolution, isotope-enabled climate model over the tropical Andes. We found out that particularly deep convection leads to the most negative values, whereas stratiform rain and shallow convection are related to less negative, even slightly positive isotope values. Consequently, it is unavoidable to consider the subclasses shallow and deep convection separately, which is why we suggest a shallow and deep convective fraction for analyzing the effect of rain types on the isotopic signal.

Keywords

Stable Water Isotopes – Precipitation – High-Resolution, Isotope-Enabled Climate Modeling – Tropical South America – Ecuador – Convection

1 Introduction

The stable isotopes of oxygen and hydrogen can be used to reconstruct past changes in the hydrological cycle based on the isotopic signals conserved in climate archives like ice cores, lake or ocean sediments and tree rings (Dee et al., 2023; Gat, 1996; Hoffmann et al., 2003; McCarroll & Loader, 2004; Thompson et al., 2000). To improve the reliability of such reconstructions a thorough understanding of the atmospheric processes influencing the isotopic composition of precipitation is necessary.

The stable oxygen and hydrogen isotope ratio of precipitation ($\delta^{18}O_P$ and δD_P, respectively) is defined as the ratio of the heavier (^{18}O, ^{2}H or D) to the lighter isotope (^{16}O, ^{1}H) with respect to standard mean ocean water or to the Vienna Standard Mean Ocean Water (VSMOW). The lower saturation vapor pressure and the heavier mass of the rare water molecules (so called isotopologues) result in a preferential accumulation of lighter isotopes in water vapor whereas the heavier isotopes tend to stay in the liquid phase. In the atmosphere, this separation, called fractionation, occurs during phase changes and is related to equilibrium (e.g. condensation) and kinetic or non-equilibrium (e.g. evaporation or deposition of vapor on ice crystal) fractionation (Ciais & Jouzel, 1994; Dansgaard, 1964).

Deuterium excess (d-excess) in precipitation describes the linear relationship between $\delta^{18}O_P$ and δD_P (d-excess = $\delta D_P - 8 * \delta^{18}O_P$) and is an indicator of non-equilibrium fractionation (Dansgaard, 1964). It reflects the atmospheric conditions (relative humidity, sea surface temperature) at the moisture sources of precipitation (Fröhlich et al., 2002; Merlivat & Jouzel, 1979; Pfahl & Sodemann, 2014), in-cloud ice formation processes (Ciais & Jouzel, 1994) or can serve as an indicator of continental moisture recycling e.g., sub-cloud evaporation of raindrops (Aemisegger et al., 2015; Graf et al., 2019) or evapotranspiration (Aemisegger et al., 2014; Ampuero et al., 2020; Fröhlich et al., 2002).

In the tropics and particularly in marine environments, the so called ‚amount effect' is observed, i.e. increasing rain amounts are related to precipitation with low $\delta^{18}O_P$ values (Dansgaard, 1964). However, the mechanisms behind the amount effect are complex and not fully understood. It can partly be explained by the preferential removal of heavy isotopes from the in-cloud water vapor during condensation. The remaining lighter water vapor forms the basis for the following condensate and leads to a subsequent depletion of precipitation (Gat, 1996). This is intensified by recycling effects in downdraft, i.e. evaporation of the falling rain and diffusive exchanges with the ambient water vapor lead to a further depletion of the water vapor, which is injected into the sub-cloud layer feeding the convective system (Risi et al., 2008).

Precipitation formation pathways can be classified into convective and stratiform. Stratiform precipitation is typically associated with low rain rates and small upward velocities or descending air below the cloud base. Convection, in contrast, features strong updrafts and high rain rates (Houze, 2014; Mölders & Kramm, 2014). In the tropics, convection often co-occurs with stratiform rain in so called mesoscale convective systems (MCSs) (Houze, 2004). These have extents on the order of 100 km and are responsible for a large proportion of annual rainfall in the tropics (Feng et al., 2021; Prein et al., 2022). The stratiform area of MCSs is fed by mid-level inflow layers from the convective area. The melting at the 0°C atmospheric thermocline (atmospheric melting layer) leads to cooling and hence to descending motions below the melting layer. Slightly ascending air is usually recognized above the melting layer (Houze, 2014).

In recent studies, the depleting effect of different rain types on stable isotopes of water vapor and precipitation has been intensely discussed (Aggarwal et al., 2016; Kurita, 2013; Kurita et al., 2011; Lekshmy et al., 2014; Munksgaard et al., 2019; Tharammal et al., 2017). An observational study in southern India found a relationship between the depleted $\delta^{18}O_P$ of collected precipitation and the activity of MCSs (Lekshmy et al., 2014). Other studies pointed out that particularly the stratiform precipitation within these MCSs is associated with a depleted $\delta^{18}O_P$ signal, which was confirmed by a conceptual model (Kurita, 2013; Kurita et al., 2011) and, in addition, by a significant negative correlation between measured monthly $\delta^{18}O_P$ and the stratiform fraction of precipitation (Aggarwal et al., 2016). This relationship could also be shown on a daily basis, however, some stations surprisingly revealed a positive correlation (Munksgaard et al., 2019). These contrasting correlation signs were also present in modeling studies with isotope-enabled general circulation models (GCMs) (Hu et al., 2018; Tharammal et al., 2017). Uncertainty arises due to the unavoidable parameterization of convection and thus simplified microphysical representation of convective rain formation in GCMs owing to their coarse spatial and temporal resolutions, which is why these models cannot fully reproduce the impact of the variability of convective systems (Houze et al., 2015) on precipitation isotope variability. To our knowledge, no study has yet used isotope-enabled high-resolution regional climate models in this respect, although these models can explicitly resolve convective processes - a tremendous advantage in research questions on different precipitation types.

Previous studies of the relation between the isotope signature and precipitation type in the tropics often focus on sites or model setups that are mainly considering maritime conditions (Kurita, 2013; Kurita et al., 2011; Munksgaard et al., 2019; Risi et al., 2020). Although climate proxies like tree rings or ice cores are located over land or in regions of complex topography, studies in those areas are still scarce. In this respect, the tropical Andes are of particular interest due to the contrasting air masses that approach the eastern and western flanks from the Atlantic and Pacific, respectively (Landshuter et al., 2020; Trachte, 2018). These different background states initiate different atmospheric processes, which are responsible for the formation of precipitation and in turn influence its $\delta^{18}O_P$ signal.

The goal of this study is to analyze the influence of stratiform and convective precipitation on the $\delta^{18}O_P$ of the eastern and western flanks of the Ecuadorian Andes. We use an isotope-enabled and high-resolution climate model in a real-case setup, which is highly advantageous for areas of complex topography and is needed to explicitly and realistically simulate convective processes.

2 Materials and Methods

2.1 Description of Study Site

The study site in southern Ecuador is determined by the complex topography of the meridionally orientated Andes (Figure 1) that act as a „climate divide“ (Emck, 2008). The western flanks and the western lowlands of Ecuador are affected by the Pacific and exhibit one clearly distinct rainy season from January to April (Garcia et al., 1998; Pucha-Cofrep et al., 2015; Volland-Voigt et al., 2011). In contrast, the Andes in this region, show a bimodal precipitation pattern with maxima in March to April and October to November (Garcia et al., 1998). The Amazon is located east of the climate divide and is influenced by air masses from the Atlantic. Precipitation in the Amazon falls during all months of the year with slightly higher amounts during March and April (Garcia et al., 1998).

The seasonal variation of the so-called Intertropical Convergence Zone (ITCZ) is an important feature determining the precipitation amounts in Ecuador. It propagates southward around November, reaches its most southern position in January and passes Ecuador again during its northward displacement from January to May. Stable isotope analysis of precipitation in Ecuador pointed out that the passage of the ITCZ is, besides topographic forcing from the Andes, a major mechanism for depleting heavy isotopes in precipitation (Garcia et al., 1998). In addition, the El Niño Southern Oscillation (ENSO) phenomenon is responsible for the high inter-annual variability of precipitation (Capotondi et al., 2015; McPhaden et al., 2006).

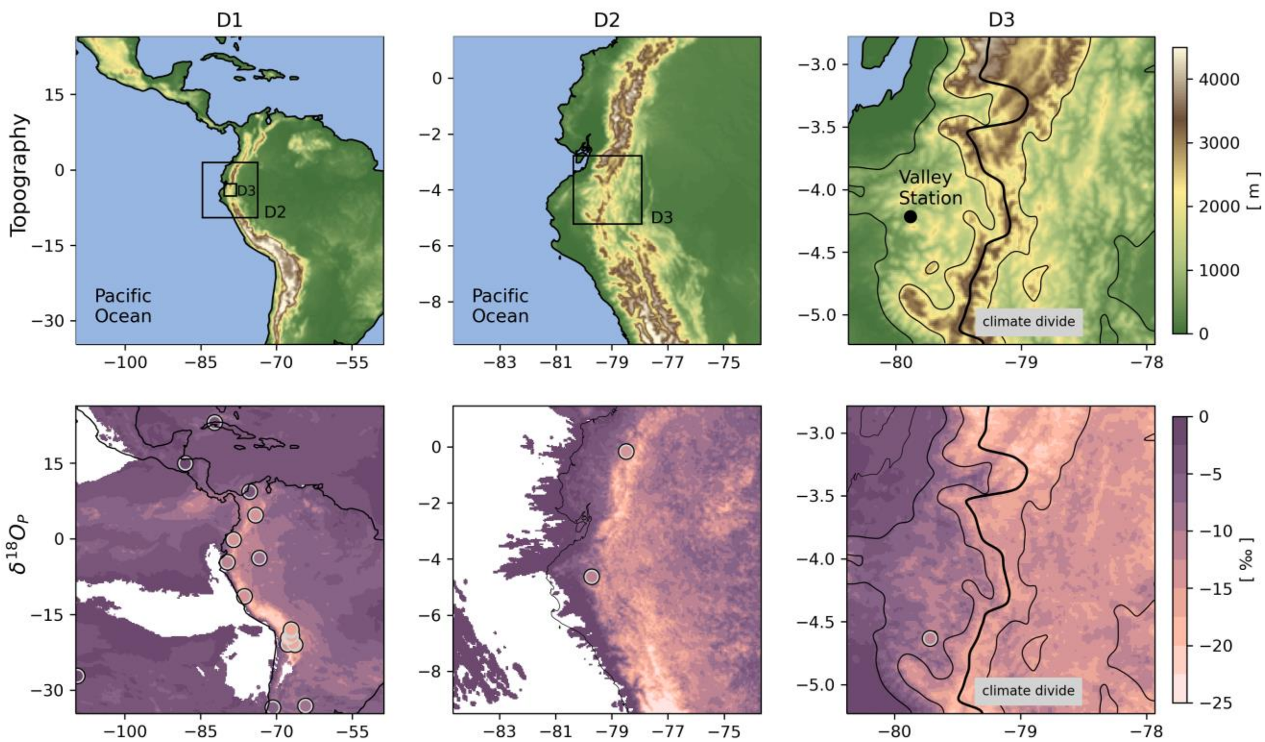

Figure 1. Topography of the study region and domain setup of the isotope-enabled version of the high-resolution climate model from the Consortium for Small-Scale Modelling ($COSMO_{iso}$) (first row). Seasonal rain rate weighted mean $\delta^{18}O_P$ of $COSMO_{iso}$ evaluated against seasonal mean observations of the Global Network of Isotopes in Precipitation (GNIP) for the same period (January 2012 to April 2012, framed circles with color representing the $\delta^{18}O_P$ of the respective station) (second row). No data is available for white areas, which can be attributed to no precipitation. Although the second row shows results that are only discussed in Section 3, we include these maps here due to the topography dependency of these results.

This study is part of a project that tries to better understand the stable isotope signal in tree rings from the western flanks of the Andes in southern Ecuador (Landshuter et al., 2020). The availability of proxy data and observations at the same location is the reason for selecting this study site. However, the focus of this study is on the stable isotopes in precipitation, whereas the link to the stable isotopes of the tree rings is part of a follow-up study. We subdivided the area into four regions (Figure S1 in Supporting Information S1):

- Western Lowlands: below 500 m and west of the climate divide
- Western Flanks: above 500 m and below 2000 m and west of the climate divide
- Andes: above 2000 m
- Amazon: below 2000 m and east of the climate divide.

We limited the analyzed time period to the rainy season from January to April of 2012 due to the computational costs and our focus on process understanding, which can be studied more efficiently in case-study frameworks than from very long records (e.g., Mölg et al., 2012). The examined months show enhanced precipitation amounts compared to the rest of the year in all defined regions. We chose the year 2012 as it was a year with moderate to high, but not exceptionally high precipitation anomalies (Landshuter et al., 2020) that are linked to anomalously warm sea surface temperatures in the eastern Pacific (Su et al., 2014).

2.2 Observations

2.2.1 Automatic Weather Station Data

Automatic Weather Stations (AWS) data was used from a deployment during a field campaign from April 2007 to March 2015. The AWS were located in „Laipuna Valley“ (590 m above sea level, -4.215°S, 79.885°W, Valley Station) and on „Laipuna Mountain“ (1,450 m above sea level, -4.238°N, 79.899°W, Mountain Station) and recorded air temperature (at 2 m), relative humidity (at 2 m), incoming short wave radiation (at 2 m), wind speed and direction (at 2 m) and precipitation (at 1 m) above the ground at 10-min intervals that were stored as hourly means (Landshuter et al., 2020; Pucha-Cofrep et al., 2015; Spannl et al., 2016; Volland-Voigt et al., 2011). To eliminate the temperature dependence of relative humidity, we also calculated and used the water vapor pressure (Marshall & Plumb, 2008; Mölders & Kramm, 2014). Particularly, the Valley Station was used to find a suitable model setup and to evaluate atmospheric variables of the model output. The Mountain Station served as a reference for the variability that can be expected nearby.

2.2.2 Satellite Retrievals

The MODerate resolution Imaging Spectroradiometer (MODIS) precipitable water product is based on retrievals from the TERRA and AQUA satellites. The Level 2 dataset, which reflects the column water-vapor amounts at 1 km spatial resolution during the day, is based on a near-infrared algorithm (Gao, 2015). We used all available images from January 2012 to April 2012 of this satellite product to calculate its time mean for an independent spatial evaluation of the modeled hydroclimate. The TERRA satellite passes the study region between 10:00 and 12:00 local time, whereas the AQUA satellite collects data between 13:00 and 15:00 local time. In total 201 images were used covering the period from January 2012 to April 2012.

2.2.3 Stable Isotope Data From Precipitation

Monthly $\delta^{18}O_P$ data were downloaded from the Global Network of Isotopes in precipitation (GNIP) database (IAEA/WMO, 2023). We selected all stations located in the study area that provided at least three of the four monthly $\delta^{18}O_P$ values (from January to April 2012), which resulted in twelve stations, for evaluating the $\delta^{18}O_P$ output of the isotope-enabled regional climate model.

2.3 Isotope-Enabled High-Resolution Climate Model

The non-hydrostatic, limited-area numerical weather and climate model from the Consortium for Small-Scale Modelling (COSMO) is based on an Arakawa C-grid on a rotated geographical coordinate system in the horizontal and can be used with terrain-following Gal-Chen height coordinates that flatten towards the top of the model domain (Steppeler et al., 2003). Numerically the model is integrated with a third order Runge-Kutta scheme with the total variation diminishing variant (Liu et al., 1994).

Its isotope-enabled version $COSMO_{iso}$ (Pfahl et al., 2012) that we used in our study, encompasses two additional parallel water cycles for each of the heavy isotopes ($H_2^{18}O$, HDO).

These water cycles do not affect other model components and can be interpreted as an individual copy of the usual water cycle of the light water molecule (H_2O) apart from fractionation processes during phase changes. No fractionation occurs in $COSMO_{iso}$ during plant transpiration (Aemisegger et al., 2015). Fractionation processes during soil evaporation are account for by TERRAiso, an isotope-enabled prognostic multilayer soil model that is coupled to $COSMO_{iso}$ (Christner et al., 2018). $COSMO_{iso}$ has previously been used in numerous different studies (Aemisegger et al., 2015; Breil et al., 2020; Christner et al., 2018; Lee et al., 2019; Pfahl et al., 2012; Thurnherr et al., 2021) including tropical and subtropical regions (de Vries et al., 2022; Villiger et al., 2023).

In our study, we employed $COSMO_{iso}$ for the first time over the complex topography of the Andes in tropical Ecuador, South America. We used a one-way nesting with a parent-to-child grid ratio of about three or five resulting in three domains of 22.5 km (~ 0.2025°, 330x330 grid cells), 4.5 km (~ 0.0405°, 300x300 grid cells) and 1.5 km (~ 0.0135°, 210x210 grid cells) grid spacing centered over southern Ecuador (-4.0000°N, 79.1500°W); these domains are hereafter referred to as D1, D2 and D3, respectively (Figure 1). The model runs were performed with 50 levels in the vertical from 1 January 2012, 06:00:00 local time until 30 April 2012 18:00:00 local time and stored with an hourly temporal resolution. The spin-up time of 48 hours was discarded for further analysis, which is why the analysis time interval starts on the 3 January 2012, 06:00:00 local time. The increasing resolution from D1 to D3 requires modifications in the setup. We thus adjusted the time step, turbulent length, orography data and the width of the relaxation layer for each domain (Table 1).

Table 1. $COSMO_{iso}$ setup for resolution-dependent parameters with orography from the Global Land One-km Base Elevation Project (GLOBE) and the Advanced Spaceborne Thermal Emission and Reflection Radiometer (ASTER).

Domain	**Resolution**	**Number of Grid Cells (lon x lat)**	**Time Step (dt)**	**Turbulent length (tur_len)**	**Relaxation Layer (rlwidth)**	**Orography**
D1	22.5 km (~ 0.2025°)	330x330	120 s	430 m	225 000 m	GLOBE (NOAA/NGDC)
D2	4.5 km (~ 0.0405°)	300x300	20 s	180 m	45 000 m	ASTER (METI/NASA)
D3	1.5 km (~ 0.0135°)	210x210	9 s	130 m	15 000 m	ASTER (METI/NASA)

The time steps are chosen to maintain the Courant number and are approximately linearly interpolated based on the spatial resolution thereby fulfilling the storage interval (3600 s) being a multiple of the time step (e.g. 120 s for D1). The asymptotic turbulent length (tur_len) is reduced to account for increasing turbulent fluxes with increasing resolution. This modification leads to steeper vertical gradients and enhanced instability in the boundary layer, which favors the initiation of convective processes (Baldauf et al., 2011). We followed the linear distribution as suggested by Vergara-Temprado et al. (2020).

Orographic features are highly dependent on the resolution, which is why we chose the orography from the Global Land One-km Base Elevation Project (GLOBE) for D1 and the finer resolved Advanced Spaceborne Thermal Emission and Reflection Radiometer (ASTER) orography for D2 and D3. Both were provided by the External Parameters for Numerical Weather Prediction and Climate Application (EXTPAR) (Asensio et al., 2020).

Lateral boundary information is transferred via the boundary zone (four grid cells at each boundary of the subdomain) and the relaxation layer. The width of the relaxation layer (rlwidth) should be 10 to 15 times the grid cell resolution in meters (Schättler et al., 2013). In our setup, we applied this requirement and used the ten times the grid cell resolution requirement for all domains. The grid cells of the boundary and relaxation layer are discarded for the data analysis.

The physical parameterization schemes that we used in our study are as follows: heating rates by radiation are calculated once per hour by the scheme of Ritter and Geleyn (1992); vertical turbulent diffusion is based on a 1-D prognostic equation for turbulent kinetic energy (Mellor & Yamada, 1974); and microphysics of cloud and precipitation are represented with the one-moment cloud ice scheme, which considers water vapor, cloud water as well as ice, rain and snow (graupel and hail are not taken into account) (Doms et al., 2011). Regarding the parameterization of convection for different spatial resolutions, there are different approaches used and debated in the literature. While some argue that 7 km resolution or even less require a parameterization (Fosser et al., 2015), others suggest that the explicit calculation or only parameterized shallow convection is advantageous up to 25 km resolution (Vergara-Temprado et al., 2020). After thoroughly testing different convection setups in terms of resolution, the following one revealed the most realistic performance. In D1, we parameterized convection using the Tiedtke (1989) scheme due to its coarse resolution. For D2 and D3, an explicit treatment of convection yielded the most realistic accumulated precipitation amounts and precipitation rates. The stable isotopes are only incorporated in the Tiedtke (1989) scheme, which is why other parameterization schemes such as only for shallow convection could not be applied.

Spectral nudging was conducted for zonal and meridional winds above 850 hPa only for D1 to constrain drift in the large-scale circulation but allowing a freely evolving atmosphere in D2 and D3. The height of the damping layer was adjusted to 18000 m (instead of 11000 m) as proposed for a tropical setup of COSMO (Panitz et al., 2014). At this height the damping is zero and increasing along a cosine damping profile to its maximum at the top of the model domain (Schättler et al., 2013).

The atmospheric and stable isotope initial and boundary data were taken from ECHAM6-wiso with temperature, vorticity, divergence and surface pressure fields nudged towards ERA5 (Cauquoin & Werner, 2021). The dataset has a spectral resolution of T127L95 (corresponding to approx. 0.9° × 0.9° horizontal resolution and 95 vertical levels) and a 6-hourly temporal resolution. In this study and for all analyses, we calculated the rain rate weighted mean of $\delta^{18}O_P$ to be consistent with $\delta^{18}O_P$ of collected rain samples (Breil et al., 2020; IAEA/WMO, 2023).

The model runs were performed on the Fritz compute cluster at the Erlangen National High Performance Computing Center (NHR@FAU) and was compiled with Intel 17.0 compilers. The final model run required about 40,000 core hours and the hourly output for all three domains encompasses roughly 3.3 TB of data.

For the evaluation, we considered the boxplots for different meteorological variables on an hourly and daily basis. The whiskers comprise 1.5 times the interquartile range. Moreover, we calculated the Pearson correlation between the variables of the $COSMO_{iso}$ output and the Valley Station, except for precipitation, where we used the Spearman correlation, because the data is not normally distributed. From these, we determined the coefficient of determination (R^2) and the significance by their *p*-values. Furthermore, we calculated the root mean square error (RMSE) and the mean bias. The heights of the $COSMO_{iso}$ output correspond to the heights of the Valley Station for all variables apart from wind. The $COSMO_{iso}$ wind variable was initially output at 10 m. For comparability with the AWS wind data, the $COSMO_{iso}$ wind was interpolated to 2 m assuming a logarithmic wind speed profile (Allen et al., 1998) .

2.4 Rain Type Classification

A common approach to distinguish convective and stratiform precipitation is the use of the Tropical Rainfall Measuring Mission (TRMM) satellite data and algorithm (Aggarwal et al., 2016; Funk et al., 2013; Schumacher & Houze, 2003). In stratiform regions a so called ‚bright band‘ occurs just below the melting layer and describes a horizontal layer of 500 m thickness with high radar reflectivity values. In contrast, convective regions are characterized by a vertically extending core of maximum reflectivity (Houze, 2014). The spatial and temporal resolution of the TRMM product is, however, too coarse and therefore not suitable for our study. In GCMs the separation arises from the convection parameterization. This means that all precipitation calculated within the parametrization scheme is classified as convective and the explicitly calculated one is classified as stratiform. With increasing spatial resolution, the climate model can resolve convective processes, leading to a misclassification of convective precipitation as stratiform rain. Consequently, a specifically tailored separation technique for stratiform and convective precipitation is needed for high-resolution models. We followed the approach of Sui et al. (2007) that is based on cloud microphysical processes expressed as ratio of the integrated ice and liquid water path (IWP and LWP, respectively). Particularly, the cloud ratio is defined as IWP/LWP, with IWP being the sum of the vertically integrated mixing ratios of all ice species (Qsnow + Qice in our case), and LWP being the sum of the vertically integrated mixing ratios of all liquid particles (Qcloud + QRain). Consequently, the cloud ratio can be interpreted as the relative importance of ice and liquid hydrometeors in clouds. Precipitation is classified as

- **Convective**, if the cloud ratio is < 0.2 (to account for high rain rates, i.e. high LWP) or if $IWP > IWP_{threshold}$ (for particularly high ice contents)
  The $IWP_{threshold}$ is the mean of IWP plus one standard deviation of IWP
  (here: $IWP_{threshold}= 2.31$ mm)
- **Stratiform**, if the cloud ratio is > 1.0 (to make sure that ice exists, but is related to low rain rates, i.e. low LWP).
- **Mixed**, for all remaining precipitation.

A distinct, process-based consideration of each class is an essential part of this study, which is why we additionally separated the convective class into shallow (cloud ratio < 0.2) and deep ($IWP > IWP_{threshold}$) convection. A discussion of this nomenclature is included in the results section (see Section 3.2.2). Sui et al. (2007) regarded the mixed class as belonging to stratiform rain, which we adopted for our study. Consequently, we refer to the subclasses of stratiform rain as mixed and strictly stratiform. This rain type classification highlights the importance of ice and snow with respect to the liquid particles for stratiform precipitation (Sui et al., 2007) (Figure S2 in Supporting Information S1). To evaluate the classification of the rain types, we considered the distribution of rain rates with respect to their fractional contribution to the overall precipitation amount (Klingaman et al., 2017).

For the stratiform fraction, we followed different other studies (Aggarwal et al., 2016; Hu et al., 2018) and calculated it as fraction of the sum over all rain rates of the stratiform and mixed class to the sum over all rain rates. For very small rain rates the stratiform fraction might be misleading, which is why we only considered hours with a total rain rate > 0.03 mm. Such a threshold is commonly also applied when using the $\delta^{18}O_P$ of the $COSMO_{iso}$ output (Pfahl et al., 2012).

3 Results and Discussion

3.1 Evaluation of $COSMO_{iso}$ and the Rain Type Classification

In the following, we present an evaluation of $COSMO_{iso}$ to ensure a realistic performance of the model regarding the hydrometeorological variables and the stable water isotopes. Thereafter, the classification method for the different rain types is evaluated. For this evaluation, we consider the distributions of rain rate contributions to the overall precipitation amount.

3.1.1 Hydrometeorological Variables

We adjusted the $COSMO_{iso}$ setup and evaluated its output with AWS data of the Valley Station by selecting the closest grid cell to this station. The Mountain Station serves as a reference for the variability that can be expected nearby (for orientation: the closest grid cell to the Mountain Station is two grid cells south and one grid cell west of the closest grid cell to the Valley Station; model output from this grid cell is not used for adjusting the $COSMO_{iso}$ setup and also not for the statistical evaluation). We chose this location at the western flanks of the Andes, because tree ring material for stable isotope analysis were collected close to the Valley Station. In a follow-up study, we want to explain these tree ring signals by using the $COSMO_{iso}$ output.

The hourly and daily temperature at 2 m is realistically captured (Figure 2) with a significant correlation and a R^2 of 0.75 for hourly values. It decreases to 0.11 for daily values due to the removal of the daily cycle by the calculation of the mean. However, this temporal aggregation leads to a decrease of the RMSE from 1.7 °C to 1.04 °C from hourly to daily, respectively. The performance resembles the one in other atmospheric modeling studies with a similar setup (convection-resolving, mountain environment, AWS data as observations, simulation period from a few days to a few months). For example, for the complex topography of the New Zealand Alps values for temperature at 2 m of 2.64 °C and 0.88 for the hourly RMSE and the R^2, respectively, were reported (Kropač et al., 2021). For a study of Foehn in Patagonia, Temme et al. (2020) obtained an hourly RMSE from 1.72 to 3.63 °C (depending on foehn event and AWS site) and a maximum R^2 of 0.77. And for a tropical high mountain in Africa, (Collier et al., 2019) obtained 0.34 for the daily R^2 and a mean deviation (comparable to RMSE) of 0.4 °C. Modelled shortwave radiation does not capture the highest observed values, resulting in a RMSE of 157.92 W/m^2 for hourly values, which is reduced to 53.94 W/m^2 for daily ones. This is again in accordance with the other studies; in the New Zealand case, the hourly RMSE of incoming shortwave radiation came to 73.94W/m^2 (Kropač et al., 2021), while the absolute mean deviation in the Africa study for daily values was 42.8 W/m^2 (Collier et al., 2019). Temperature at 2 m and shortwave radiation of the Mountain Station considerably differ from those of the Valley Station that is located nearby. This is to be expected in areas of complex topography. However, the fact that $COSMO_{iso}$ realistically reproduces temperature at 2 m and shortwave radiation at the Valley Station in this region of high spatial variability is, therefore, encouraging.

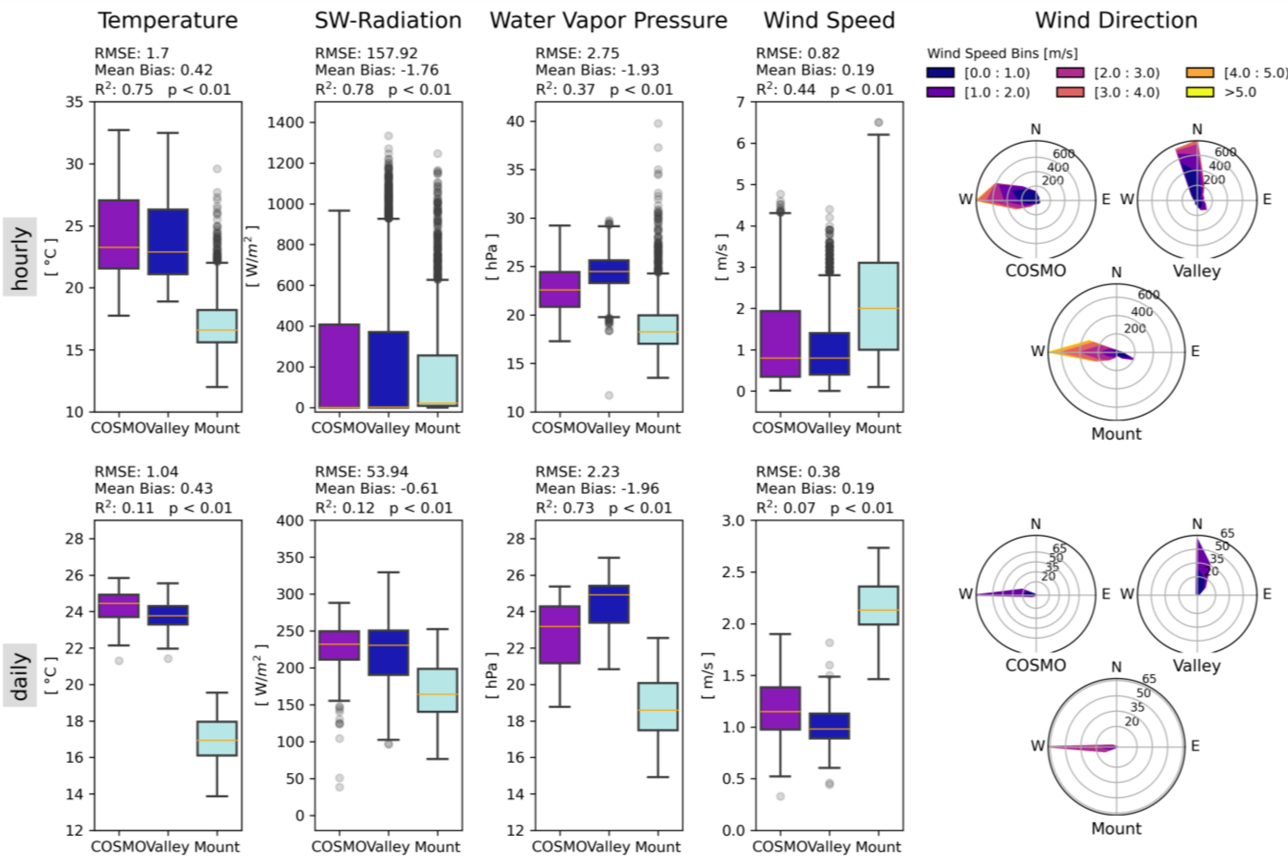

Figure 2. Evaluation of $COSMO_{iso}$ temperature at 2 m (first column), shortwave radiation at the surface (second column), water vapor pressure at 2 m (third column), wind speed at 2 m (fourth column) and wind direction at 2 m (wind roses) against Automatic Weather Station (AWS) data (Valley and Mountain Station) for hourly (upper row) and daily (lower row) values The Root Mean Square Error (RMSE), Mean Bias and Coefficient of Determination (R^2) are calculated between the $COSMO_{iso}$ output and the Valley Station.

The humidity expressed as water vapor pressure, is slightly underestimated (mean bias for daily and hourly about -1.9 hPa) but the mean is clearly closer to the Valley Station than to the Mountain Station. The mean bias of wind speed is small with 0.19 m/s for both temporal resolutions and $COSMO_{iso}$ again manages to represent conditions at the Valley Station in a realistic way, but not the ones at the Mountain Station. While the other studies cited above are harder to compare for these two variables in terms of absolute values (either because they used different measures of air humidity, or they decided on a different evaluation strategy for wind speed concerning the reference height), our metrics lie within their performance ranges for variability. For example, they demonstrate hourly R^2 to vary substantially from 0.14-0.72 (0.37 in our case) for humidity (Kropač et al., 2021; Temme et al., 2020), and a maximum of 0.52 (0.44 in our case) for wind speed (Kropač et al., 2021).The wind direction of $COSMO_{iso}$ more closely resembles that of the Mountain Station, which is caused by the real orientation of the narrow valley where the Valley Station is located. This topographic condition is not captured by the spatial resolution of 1.5 km of D3. The same, but understandable, deviation was found in a very recent study of a high-mountain environment in New Zealand (Kropač et al. 2023, under review)

Precipitation as the focus variable of this study shows a good performance as well (Figure 3), in particular cumulative precipitation amounts align well with the Valley Station. The R^2 of hourly precipitation is expectedly low, since the exact timing of precipitation events typically differs between models and observations at such high temporal resolution (e.g., Mölg & Kaser, 2011). However, the R^2 of daily precipitation of 0.28 is even slightly better than the ones for a high-resolution model simulation over Ecuador, yielding a R^2 of 0.05 and 0.2 for an AWS at the coast and one at 2685 m altitude, respectively (Chimborazo & Vuille, 2021). Nevertheless, the promising and important aspect in the results is that high intensity precipitation events are realistically reproduced in terms of both rain rate and duration. Furthermore, the daily cycle is well captured. A study over the European Alps covering ten years found a similarly high agreement in the daily cycle (Ban et al., 2014). They could show that it resulted from the explicit representation of convection in a high-resolution setup with COSMO. However, between 9 p.m. and 1 a.m. local time, precipitation is slightly overestimated in our model, and it is slightly underestimated in the morning hours.

To evaluate the spatial hydroclimatic variability of the $COSMO_{iso}$ output, we compared the column water-vapor amounts provided by the MODIS precipitable water product to the time mean of the vertically integrated water vapor (TQV) from $COSMO_{iso}$ (Figure 3). It can be noticed that humidity is underestimated in the coastal regions. This is in accordance with the

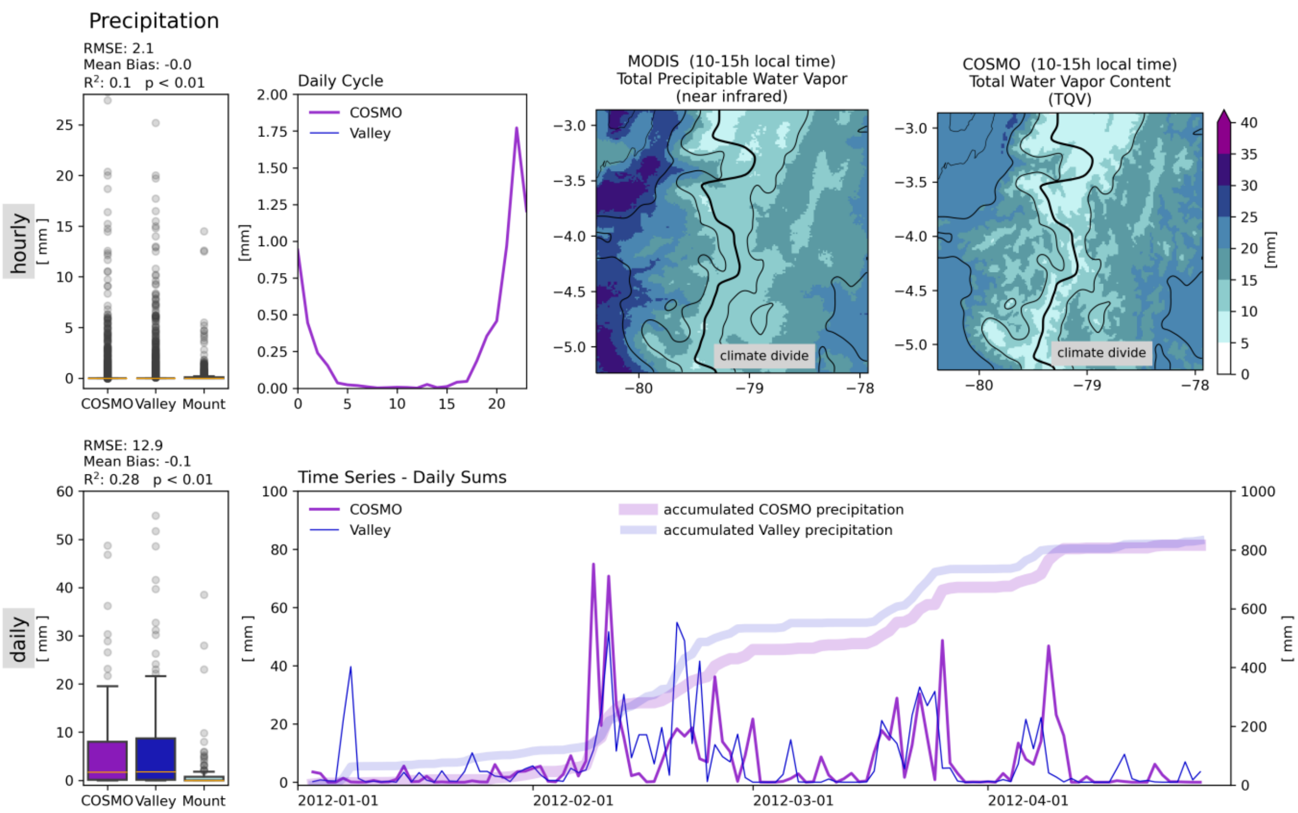

Figure 3. Evaluation of precipitation from $COSMO_{iso}$ against AWS data considering boxplots of hourly and daily sums (upper and lower panel of first column, respectively), the daily cycle (upper panel of second column) and accumulated precipitation amounts (lower panel). Spatial evaluation of total water vapor content against satellite retrievals from the MODerate resolution Imaging Spectroradiometer (MODIS) (upper right panels). The RMSE, Mean Bias and R^2 are calculated between the $COSMO_{iso}$ output and the Valley Station.

slight underestimation of humidity observed in comparison with the Valley Station. A similar underestimation of specific humidity is also found in a series of simulations over the North Atlantic trade wind region (Villiger et al., 2023). The Andes and the topographic effects are, however, well captured, giving confidence in the simulated spatial pattern. Accordingly, the spatial correlation coefficient amounts to 0.52 (p-value < 0.01).

3.1.2 Stable Oxygen Isotopes of Precipitation

Isotopic data are scarce in the vicinity of the study site and only available with a monthly resolution. Therefore, we conducted the evaluation separately for every model domain (D1, D2, D3). The monthly mean $\delta^{18}O_P$ of COSMO$_{iso}$ realistically captures the depleted signal with increasing altitude and the only slightly depleted values of central America, a result included in Figure 1 to re-call the topographic conditions of the study region. The amount effect in COSMO$_{iso}$, meaning the relationship between the hydroclimate and the stable water isotope signals, is well reproduced, which is shown by the significant daily negative correlation between daily rain sums and daily mean $\delta^{18}O_P$ (Figure S3 in Supporting Information S1).

3.1.3 Rain Type Classification

The distribution of the precipitation contribution of stratiform and convective rain rates to the total rain amount shows a maximum of the distribution of the stratiform rain rates being clearly smaller than the convective one (Figure 4a). Breaking down the classification further into strictly stratiform, mixed, shallow and deep convection (Figure 4b) emphasizes the distinct rain rate difference between deep convection and strictly stratiform rain even more. The mixed rain rates are, as expected, mostly between deep convective and strictly stratiform. The shallow convection maximum rain rates occur at lower rain rates than deep convective ones and slightly higher than mixed ones. Further confirmation for this partition method is included within the main analysis (see Section 3.2.2). Overall, the results confirm the usefulness of this classification scheme to distinguish between the different rain formation pathways.

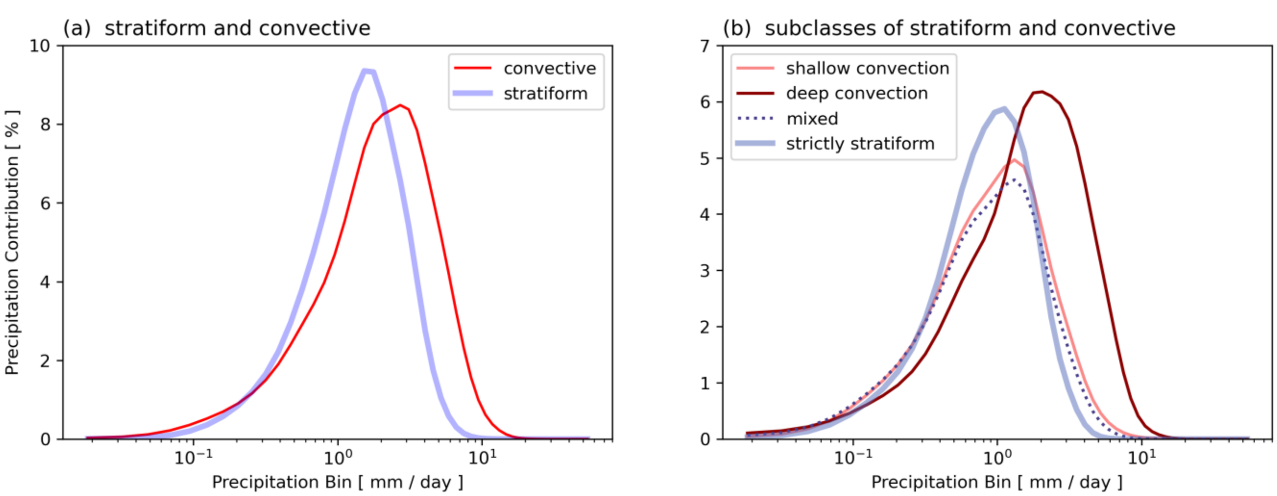

Figure 4. Contribution of each rain rate bin to the total precipitation of each rain type: convective and stratiform rain (a) and their subclasses (b). The area below each curve sums up to 100 %.

3.2 Relationship Between $\delta^{18}O_P$ and Rain Types

The main analysis starts with the consideration of the relationship between stratiform fraction and $\delta^{18}O_P$ based on model output of COSMO$_{iso}$. This is followed by a thorough investigation of the underlying processes and ends with an analysis of the variability of the occurrence of rain types in time and a suggestion for using a deep convective fraction or shallow convective fraction due to the large difference in their associated isotope signals.

3.2.1 Correlation Between $\delta^{18}O_P$ and Stratiform Fraction

The regression slope of the correlation between daily stratiform fraction and daily mean $\delta^{18}O_P$ shows a distinct east-west pattern (Figure 5a) with a negative relationship west and a positive relationship east of the climate divide. The regression slopes are significant (p-values < 0.05) only in a few regions (Figure 5b). Thereby, we additionally accounted for field significance (i.e., for spatial autocorrelation) by minimizing the false discovery rate (FDR) (Wilks, 2011). The latter strongly decreased the area of significant correlations (not shown). The R^2 (Figure 5c) is higher west of the climate divide than on the eastern side. Overall, the R^2 values are not particularly high, only a few are above 0.4. On the one hand, the small number of significant grid cells and the low R^2 values probably arise from the high temporal resolution (daily). The same observation has been made for the amount effect, which shows a similar reduced explained variance with an increased temporal resolution (Risi et al., 2008; Vimeux et al., 2005). On the other hand, the spatial extent the stratiform fraction is calculated for, is another factor. For example, Aggarwal et al. (2016) determined the stratiform fraction for a box of about 275 km x 275 km, whereas in our study, it is calculated for each grid cell (1.5 km x 1.5 km). In fact, we achieved the highest R^2 using a region-wide stratiform fraction (not shown) and

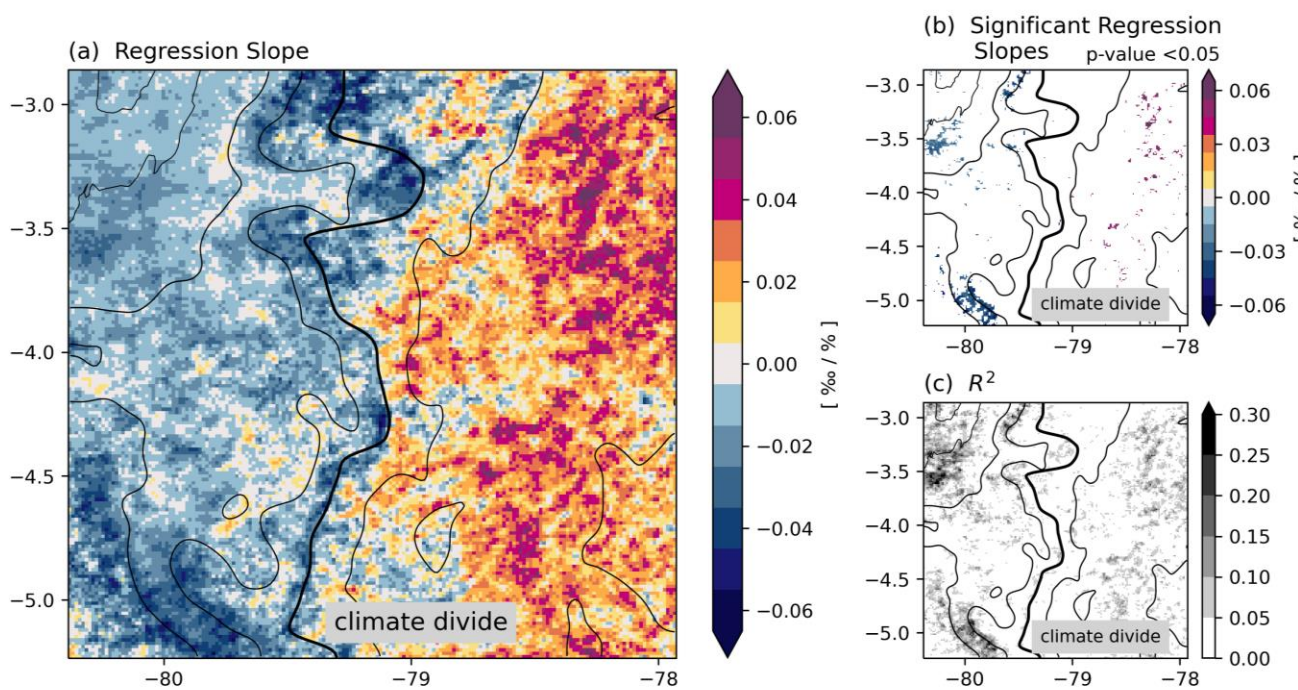

Figure 5. Regression slope between $\delta^{18}O_P$ and the stratiform fraction (a), significant regression slopes (p-value < 0.05 and additionally accounted for field significance by minimizing the false discovery rate) (b) and R^2 of the correlation (c).

similarly, Vargas et al. (2022) found the best correlation with $\delta^{18}O_P$ using region-wide precipitation. However, for a better understandability, we used the grid-cell-based calculation of the stratiform fraction.

The negative relationship west of the climate divide is consistent with a tropical to mid-latitude wide observational study using monthly GNIP station $\delta^{18}O_P$ and TRMM based stratiform fractions (Aggarwal et al., 2016). A site-specific and daily analysis covering tropical and subtropical stations further confirms this relationship (Munksgaard et al., 2019). The latter study, however, also encompasses a few stations showing a positive relationship. Generally, all stations of their study are influenced by a maritime climate, and the few continental sites were excluded from the main analysis, because of a weak relationship. Our hypothesis is that the stratiform fraction is not a good measure of rainfall formation pathways in this region. As convection is the main driver for tropical precipitation with stratiform precipitation being a consequence (MCS), we need to look closer into the different rainfall formation pathways.

3.2.2 Seasonal Mean Analysis

In search for the reason for the differing regression sign east and west of the climate divide for the relationship between the stratiform fraction and $\delta^{18}O_P$, we analyzed seasonal mean composites of different atmospheric variables. The composites are based on the rain types convective and stratiform as well as on their subclasses deep convective, shallow convective, strictly stratiform and mixed rain (see Section 2.4).

To eliminate the influence of the topography on the $\delta^{18}O_P$, which leads to a decrease of

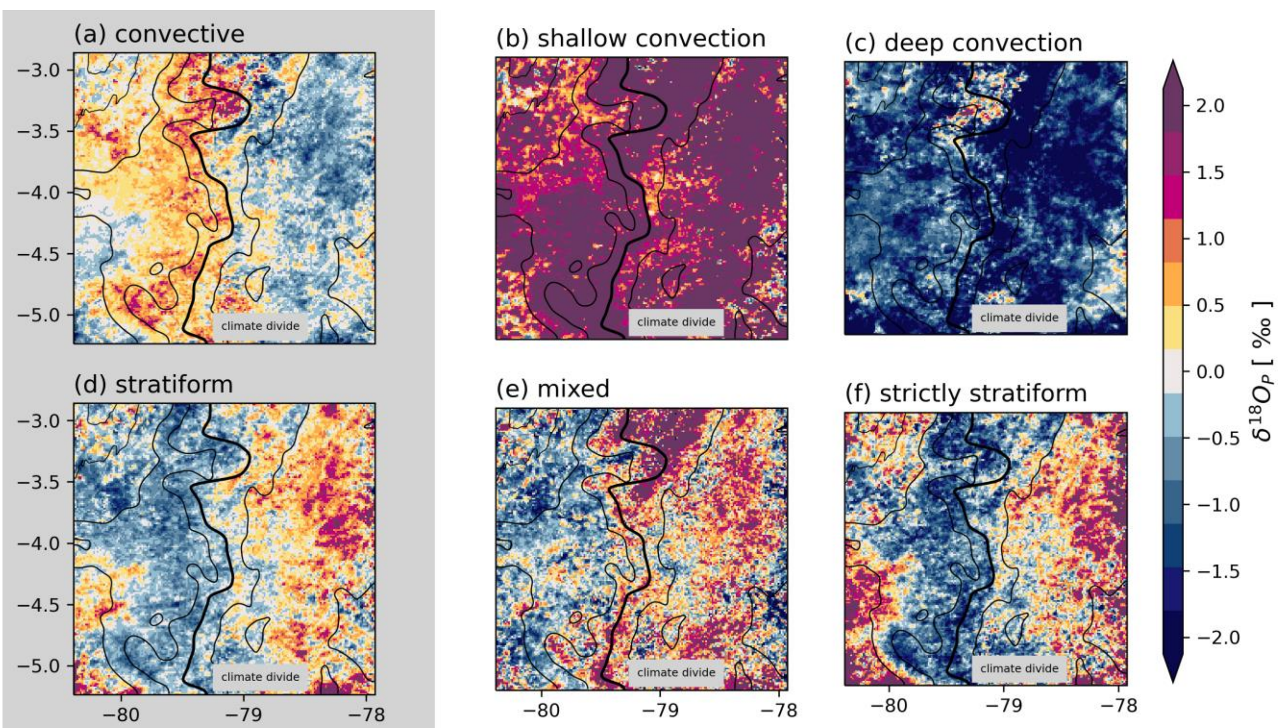

Figure 6. Seasonal mean anomaly composites of $\delta^{18}O_P$ for convective and stratiform rain ((a) and (d), respectively, grey background) and their subclasses shallow convection, deep convection, mixed and strictly stratiform ((b),(c),(e) and (f), respectively, white background).

$\delta^{18}O_P$ with altitude (Dansgaard, 1964) that would dominate the composite, we subtracted the mean over all “rainy” time steps (hours with rain >0 mm) at each grid point from the seasonal mean $\delta^{18}O_P$ at the respective grid point. This procedure is restricted to the rainy time steps, as the seasonal mean composites for each rain type, by definition, only considers rainy time steps at each grid cell. In the following, we refer to the $\delta^{18}O_P$ composite as anomaly composites and to the seasonal mean composites just as composites.

The $\delta^{18}O_P$ anomaly composites for convective and stratiform rain (Figure 6a and 6d, respectively) show a very similar east-west dipole pattern as the sign of the regression between stratiform fraction and $\delta^{18}O_P$ (Figure5). Revealing the reason for the $\delta^{18}O_P$ pattern for the convective and stratiform composites will help to understand the contrasting signs in the stratiform fraction-$\delta^{18}O_P$ relationship. The convective (first row (a-c) of Figure 6 to Figure 11) and stratiform (second row (d-f) of Figure 6 to Figure 11) formation pathway will be examined separately and in more detail in the next two sections.

3.2.2.1 Mechanisms Driving the Convective $\delta^{18}O_P$

The $\delta^{18}O_P$ anomaly composite of shallow and deep convection (Figure 6b and 6c, respectively) shows a markedly distinct signal of relatively enriched and depleted $\delta^{18}O_P$ values, respectively. In the following, we show that these differences do not only arise due to the rain type definition itself but can also be physically constrained.

Positive vertical velocities for deep convection (Figure 7c) are reaching from a few kilometers above the surface to an altitude of almost 15 km. Whereas, for shallow convection (Figure 7b), they hardly reach beyond the atmospheric melting layer. The latter is indicative for the predominant occurrence of the cloud types shallow cumulus and cumulus congestus. Together with cumulonimbus, they make up the three dominating cloud types of the tropics. Shallow cumuli and cumuli congestus reach up to heights of about 2 km and near the atmospheric melting layer, respectively, and consist only of liquid particles (Johnson et al.,

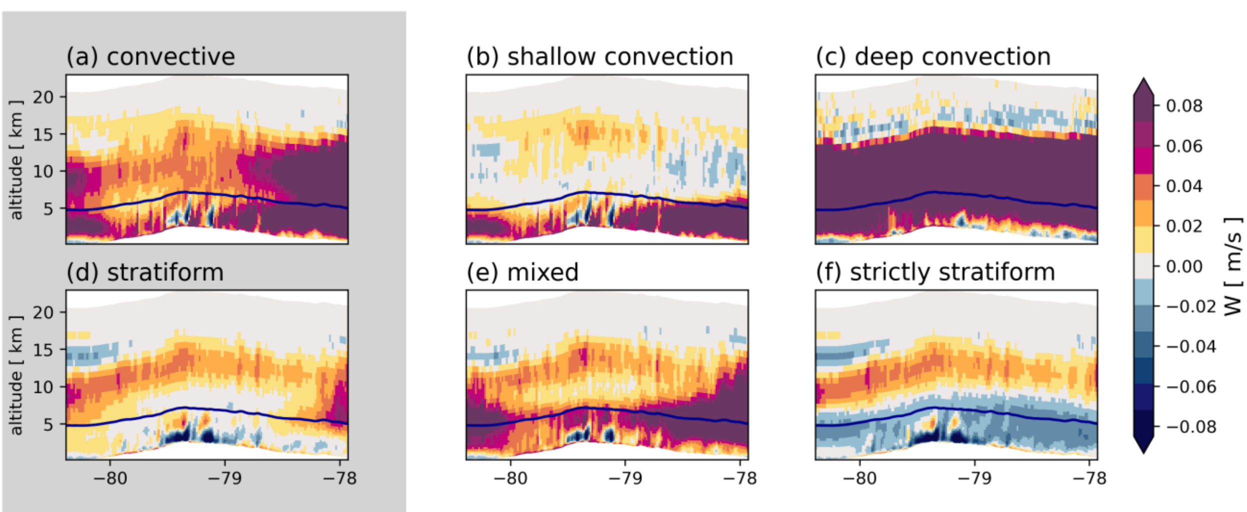

Figure 7. Seasonal meridional mean of vertical velocity for convective and stratiform rain ((a) and (d), respectively, grey background), their subclasses shallow convection, deep convection, mixed and strictly stratiform ((b),(c),(e) and (f), respectively, white background) and the seasonal meridional mean height of the atmospheric melting layer (T=0°C, bold line).

1999). This is consistent with the IWP composite (Figure S4 in Supporting Information S1), which is, by rain type definition, very low for shallow convection and very high for deep convection. In contrast, the LWP composite is high for both convective rain types; hence, leading to high rain rates (Figure S5 in Supporting Information S1). For simplicity, we use the term shallow convection, although it also comprises mid-level convection of cumuli congestus.

Low outgoing longwave radiation (OLR) at the top of the atmosphere, as an indicator for deep convection (Gao et al., 2013; Wang, 1994; Wang & Xu, 1997), mirrors the $\delta^{18}O_P$ anomaly composite of shallow and deep convection. As one would expect, very low OLR values are associated with deep (Figure 8c) and high OLR values coincide with shallow convection (Figure 8b).

Linking the $\delta^{18}O_P$ anomaly composite with the vertical velocity, IWP, LWP and OLR composites, shows that the $\delta^{18}O_P$ signals can be explained by differing microphysical and dynamical mechanisms. Additionally, this further increases the confidence in the rain type partitioning method. Hence, it is reasonable to conclude from the synthesis of data that shallow convection is related to relatively enriched $\delta^{18}O_P$ signals, whereas deep convection is related to highly depleted $\delta^{18}O_P$ values.

To explain the differing sign of $\delta^{18}O_P$ signals east and west of the climate divide for convective rainfall (Figure 6a), we calculated the fractional contribution of each class and subclass to the total seasonal precipitation amounts at each grid cell (Figure 9). West of the climate divide, shallow convection mostly contributes to seasonal precipitation amounts (Figure 9b), whereas east of the climate divide, it is the deep convection (Figure 9c). In this respect, it is noteworthy, that a little patch exists west of the climate divide that does have a high contribution

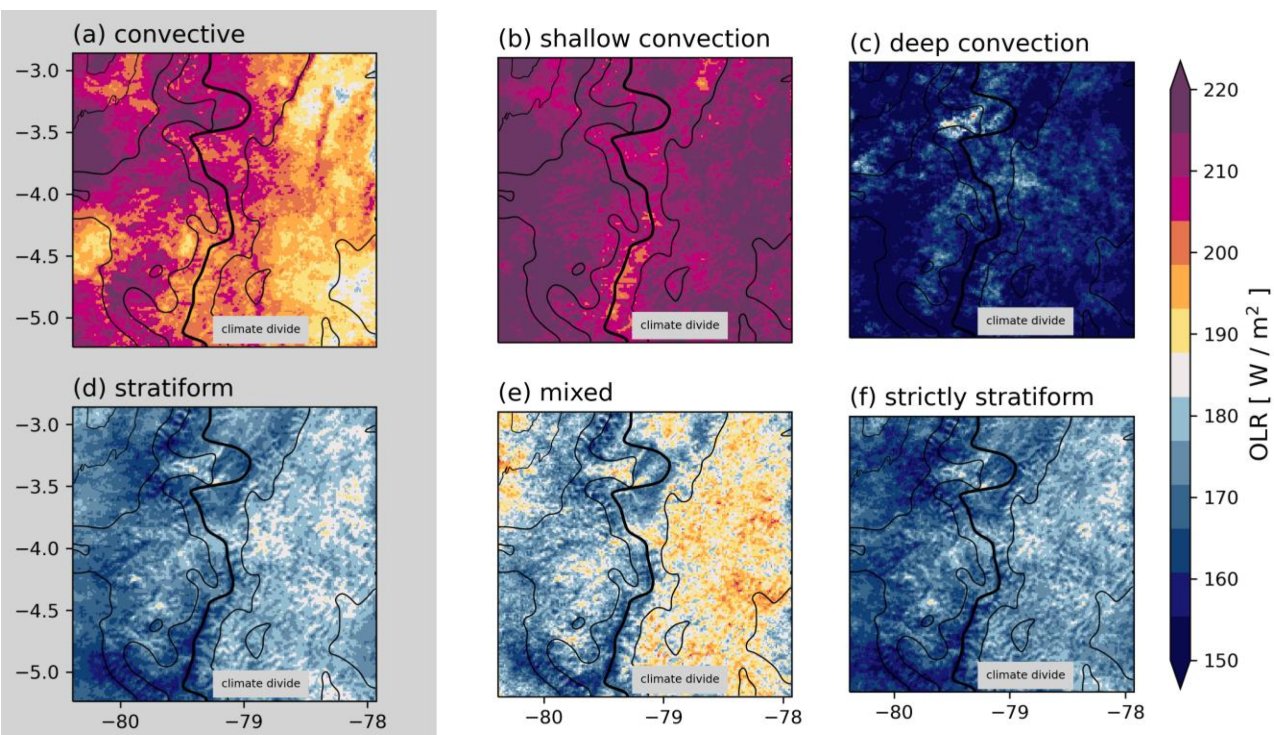

Figure 8. Seasonal mean composites of outgoing longwave radiation (OLR) for convective and stratiform rain ((a) and (d), respectively, grey background) and their subclasses shallow convection, deep convection, mixed and strictly stratiform ((b),(c),(e) and (f), respectively, white background).

from deep convection (Figure 9c). This is linked to an increasing elevation acting as a trigger for deep convection. Overall, we conclude that the relatively enriched $\delta^{18}O_P$ signal in most areas west of the climate divide arises mainly from the dominant contribution of shallow convection to seasonal precipitation amounts whereas the depleted signal east of it reflects the prevailing influence of deep convection.

The western lowlands and western flanks are in the vicinity of the Pacific Ocean, therefore, it is not surprising that shallow convection is quite pronounced as it is mainly an oceanic phenomenon (Houze et al., 2015; Lacour et al., 2018). In contrast, deep and intense convection occurs prevalently over land (Houze et al., 2015) and leads to rather low water isotope signals east of the climate divide.

3.2.2.2 Mechanisms Driving The Stratiform $\delta^{18}O_P$

The opposed west-east $\delta^{18}O_P$ gradient in the anomaly composite pattern of stratiform precipitation (Figure 6d), compared to the gradient in the $\delta^{18}O_P$ of convective precipitation, cannot be explained by differences in the $\delta^{18}O_P$ signal or the precipitation contribution between mixed and strictly stratiform. A slight difference in OLR with lower OLR values in the west (Figure 8f) coincide with and can be explained by enhanced upward velocities above the atmospheric melting layer in the west (Figure 7f). The latter together with the descending motion below the atmospheric melting layer is characteristic of stratiform circulation properties (Houze, 2014).

However, the different contributions of shallow and deep convection in the west and in

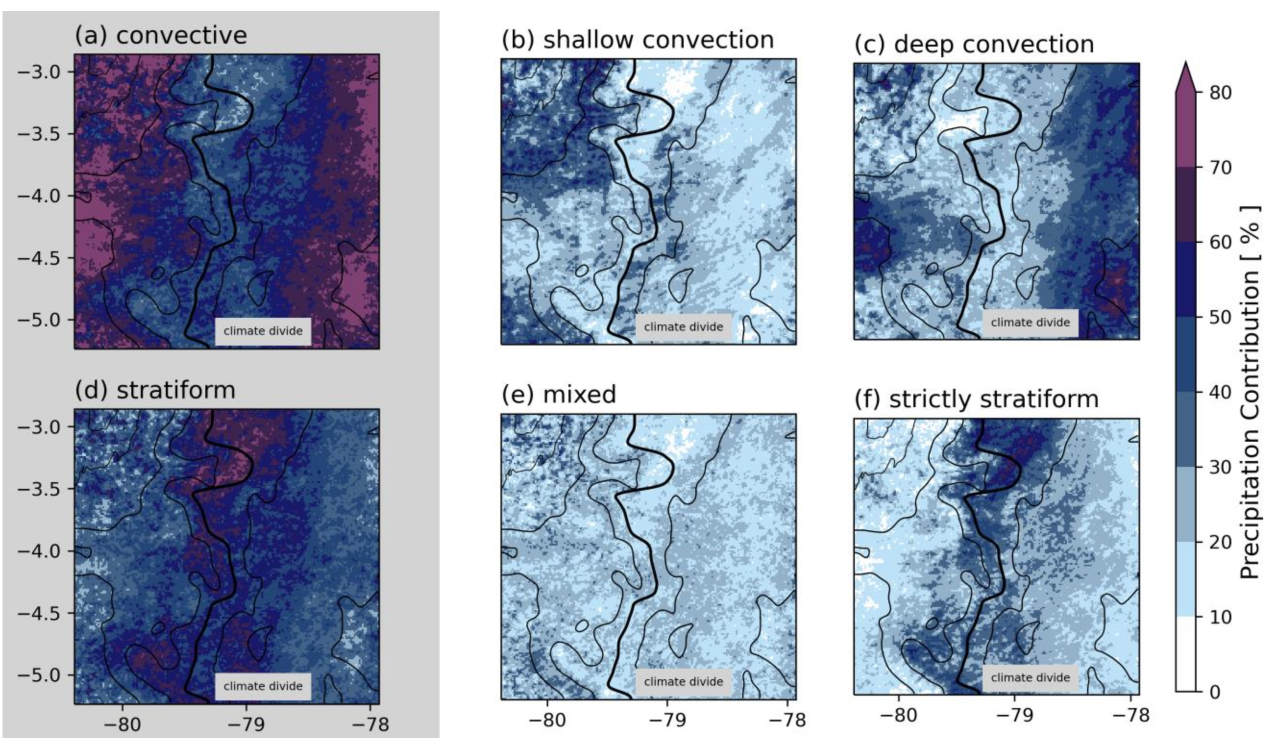

Figure 9. Precipitation contribution to seasonal precipitation amounts for convective and stratiform rain ((a) and (d), respectively, grey background) and their subclasses shallow convection, deep convection, mixed and strictly stratiform ((b),(c),(e) and (f), respectively, white background).

the east of the climate divide are more important in this context. In particular, west of the climate divide, where shallow convection is most pronounced, the intense relative enriching effect of shallow convection results in a relatively positive $\delta^{18}O_P$ sign for convective precipitation (Figure 6a) and consequently to a negative sign for stratiform precipitation, which in this region tends to originate from relatively higher altitudes than the shallow convective precipitation (Figure 6d). East of the climate divide, where deep convection dominates over shallow convection, this relationship is reversed (stratiform precipitation tends to originate from relatively lower altitudes than in deep convective systems). In the following section, we will show that the rate of depletion from stratiform precipitation is not dependent on the region, which in turn gives evidence of the described effect of the differing shallow and deep convective contributions west and east of the climate divide.

3.2.3 Strength of the Amount Effect

To clarify which rain type yields the highest depletion with rain rates, we analyzed the strength of the amount effect for each rain type. Therefore, we calculated the regression slope (Figure 10) and the R^2 (Figure S6 in Supporting Information S1) between hourly rain rate and hourly $\delta^{18}O_P$ at each grid cell for each rain type, separately. Only regression slopes smaller than -1 ‰/mm are statistically significant (*p*-values smaller than 0.05 and additionally accounting for field significance with the FDR approach, Figure S7 in Supporting Information S1). The depleting effect for shallow convection is the weakest (Figure 10b) and the one for deep convection (Figure 10c) is the most intense followed by mixed rain (Figure 10e). The amount effect for strictly stratiform (Figure 10f) is weaker than that for deep convection and over wide

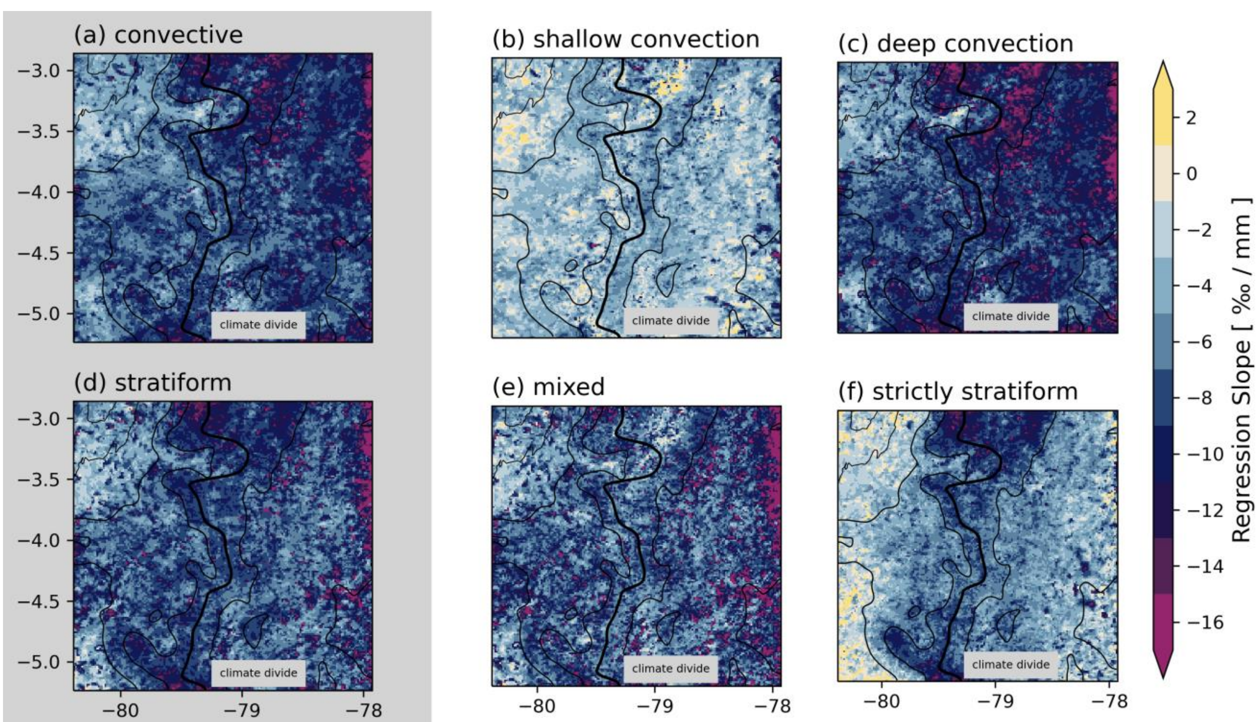

Figure 10. Strength of the amount effect – regression slope between $\delta^{18}O_P$ and hourly rain rates for convective and stratiform rain ((a) and (d), respectively, grey background) and their subclasses shallow convection, deep convection, mixed and strictly stratiform ((b),(c),(e) and (f), respectively, white background).

areas closer to shallow convection. Comparing the classes of convective (Figure 10a) and stratiform precipitation (Figure 10d) does not show a pronounced difference although clear differences arise within the subclasses. Moreover, the depleting effect of each rain type is spatially relatively uniform and independent of the region, supporting our assumption of the effect of the relative contributions of shallow and deep convection in the west and in the east of the climate divide on the stratiform anomaly composite of $\delta^{18}O_P$ (Figure 6d, see Section 3.2.2.2).

3.2.4 Influence of Rain Types on D-Excess

In addition to the results above focusing on $\delta^{18}O_P$, we considered seasonal mean composites of d-excess, which may reveal non-equilibrium effects like vapor deposition on ice in supersaturated conditions or sub-cloud rain evaporation (Figure 11). For all rain types a west-east gradient is evident with values between -5 and 15 ‰ in the west and values greater than 15 ‰ in the east, which most likely originate from the contrasting moisture source regions. West of the climate divide, the oceanic influence from the Pacific is of particular importance and leads to d-excess values of roughly 10 ‰. While the values are higher east of the climate divide, due to moisture recycling (Aemisegger et al., 2014; Ampuero et al., 2020; Fröhlich et al., 2008) that is a prominent feature within the Amazon region (Ampuero et al., 2020; Victoria et al., 1991; Zhiña et al., 2022). An altitude effect, reflecting the topography of the Andes, as found in other study regions (Gonfiantini et al., 2001; Natali et al., 2022) is not clearly detectable.

A striking feature of the d-excess composites is the exceptional high values for deep convection over the whole area (Figure 11c). The few lower d-excess values within the deep convection composite come from little rain amounts and hence precipitation contribution of less than 10 % (Figure 9) and are not representative. However, the effect of deep convective systems

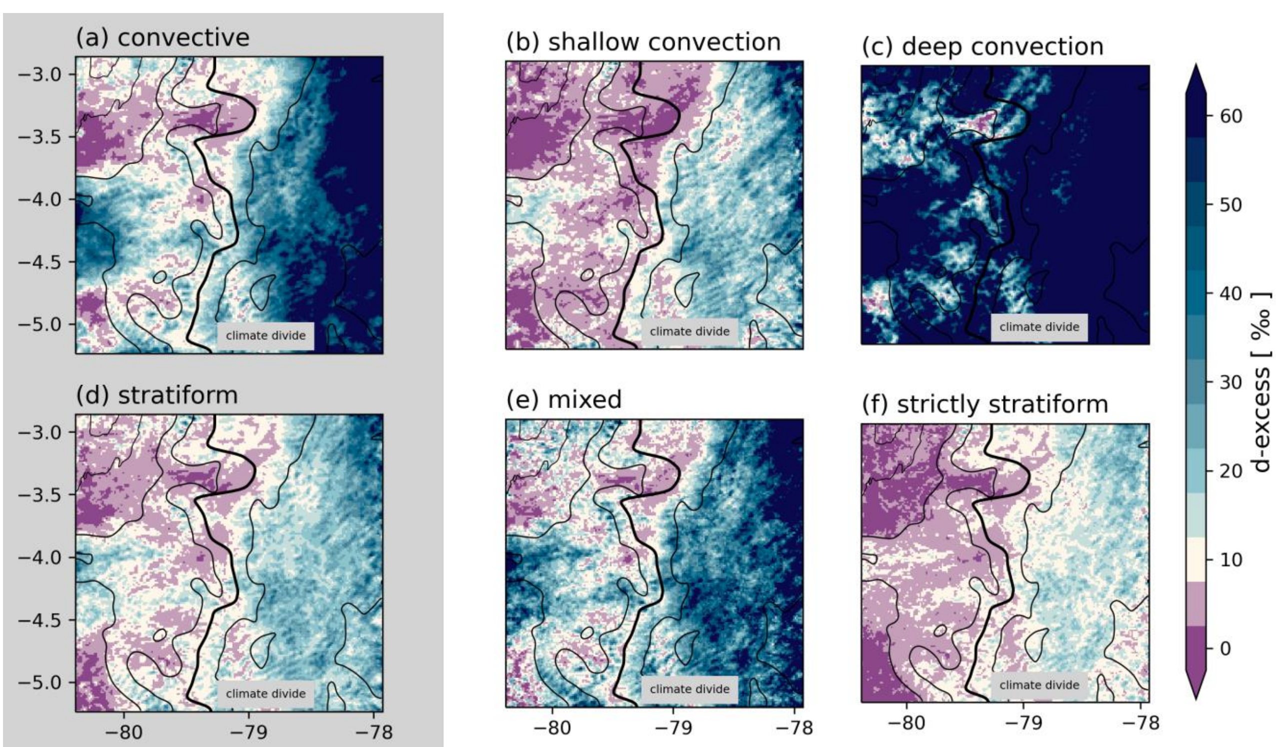

Figure 11. As Figure 8, but for deuterium excess (d-excess).

is superimposed to the effect of moisture sources. This can be seen by the region of slightly higher elevation west of the climate divide (at the left border of the map at -4.0°N to -4.5°N). It has high precipitation contributions from deep convection (Figure 9) and is related to high d-excess values despite its close location to the Pacific (Figure 11a and Figure 11c). This finding highlights the importance of the rain formation pathway on the d-excess value of precipitation and is further confirmed by the lowest d-excess values for the strictly stratiform composite.

In the following, we comprehensively discuss the $\delta^{18}O_P$ and d-excess relationship for the different rain types based on the results of the composite analysis and the amount effect in more detail. The contrasting isotopic signal of shallow and deep convection was also found within isotopic water vapor observations covering the Indian Ocean as far as the eastern Pacific (Lacour et al., 2018). Moreover, a sensitivity study with the global isoCAM3.0 at a spatial resolution of 155 km agrees with our results and shows that the strength of deep convection is related to the degree of $\delta^{18}O_P$ depletion (Tharammal et al., 2017). This can be explained by the effect of the strength of convergence (Moore et al., 2014) and a depleting effect with increasing altitude (altitude effect). The latter can be attributed to the removal of condensate by precipitation. As a consequence, the subsequent condensate forms from already depleted vapor (Dansgaard, 1964) and implies that the deeper and higher convective processes reach, the more depleted the $\delta^{18}O_P$ signal becomes. This altitude effect is further supported by the high d-excess values of deep convection, as d-excess of water vapor increases with altitude to values of 150 - 250‰ in the upper troposphere (Bony et al., 2008; Samuels-Crow et al., 2014). Moreover, we suggest that the existence of atmospheric ice and snow is of particular importance for the depletion of $\delta^{18}O_P$, as deep convection is related to the highest ice and snow contents in our study. Indeed, the fractionation for vapor-to-ice phase changes is higher than for vapor-to-liquid ones (Ciais & Jouzel, 1994; de Vries et al., 2022). Moreover, additional fractionation occurs, when the air is supersaturated over ice, but not over liquid water (supercooled water). In this case, evaporation occurs on supercooled water droplets, while its evaporate deposits on already existing ice crystals. This supersaturation mechanisms is related to non-equilibrium effects (Ciais & Jouzel, 1994; Korolev et al., 2017). As d-excess is an indicator for non-equilibrium fractionation, its high values for deep convection (Figure 11c) support our assumption of the importance of ice and snow for the depletion of deep convective precipitation. In contrast, shallow convection consists only of liquid water and the respective cloud tops are not reaching high altitudes explaining the lower depletion of shallow convection.

The less intense depletion rate of stratiform rain particularly in contrast to deep convection only partially agrees with other studies. Observational and modeling studies with a coarsely resolved GCM and a conceptual model showed a maximum depletion, when the extent of the stratiform area in a convective system yielded the greatest extent (Kurita, 2013; Kurita et al., 2011). These seemingly contradicting results can be reconciled by the given fact that the maximum in the stratiform area can be explained by a maximum in the intensity of deep convection. As they did not particularly distinguish into stratiform and convective precipitation, this seems plausible. That it is a matter of the same processes is reinforced by a maximum in d-excess accompanying the strongest $\delta^{18}O_P$ depletion in their and our results. In our strictly stratiform case we assume that sub-cloud rain evaporation does increase the $\delta^{18}O_P$ value (Aemisegger et al., 2015; Lee & Fung, 2008). This is supported by very low seasonal mean d-excess values of strictly stratiform precipitation that are caused by the decreasing effect on the d-excess value of precipitation during sub-cloud rain evaporation (Fröhlich et al., 2008). In summary, analyzing the effect of rain types on the $\delta^{18}O_P$ signal requires the consideration of subclasses and particularly, a separation between shallow and deep convection is necessary.

3.3 Occurrence of Rain Types in Time

To investigate the temporal evolution of the proportions of rain types to derive a foundation for future studies (e.g. Paleo-isotopic reconstructions), we analyzed the fractional contribution of each rain type to the daily sum of precipitation for the defined regions (see Section 2.1 and Figure S1 in Supporting Information S1): western lowlands, western flanks, Andes and Amazon (Figure 12). It clearly shows that west of the climate divide, the start of the rainy season occurs at the beginning of February and distinct high intensity precipitation events occur besides low amount precipitation events. This agrees well with other studies for tropical high mountains in South America (Bendix & Lauer, 1992; Emck, 2008; Garcia et al., 1998; Landshuter et al., 2020).

In contrast, the Amazon reveals rain events with similar intensities that frequently occur throughout the analyzed time period, which is consistent with observations (Garcia et al., 1998). However, the slightly higher precipitation amounts during March and April east of the climate divide (Emck, 2008; Garcia et al., 1998) are not detectable in our study and might be related to the short analysis time period.

In all regions, high proportions of shallow convection are associated with low daily rain amounts. Whereas great proportions of stratiform rain co-occur with deep convective ones and can be interpreted as embedded in MCSs. MCSs are a common phenomenon within the study site, irrespective of west or east of the climate divide (Bendix et al., 2003; Bendix et al., 2009; Campozano et al., 2018; Rollenbeck & Bendix, 2011; Zhiña et al., 2022).

High proportions of shallow convection are associated with more relatively enriched $\delta^{18}O_P$ values. The $\delta^{18}O_P$ decreases, particularly, with the occurrence of MCSs. This is consistent with a variety of studies (Garcia et al., 1998; Kurita, 2013; Kurita et al., 2011; Lekshmy et al., 2014; Zwart et al., 2016) and our results (see Section 3.2.2). The western regions show that after a MCS depletion event the $\delta^{18}O_P$ recovers to its seasonal mean state at around 0 ‰. In the Amazon, this recovery process is overlapped by a continuous depleting trend in the course of the rainy season, related to the high frequency of rain events. Towards the end of the rainy season, in the beginning of April, this trend is emphasized by a remarkably depleting MCS event comprising an exceptionally high fraction of deep convection. This further confirms our result that particularly deep convection leads to the highest $\delta^{18}O_P$ depletion.

As MCSs are associated with a high fraction of stratiform rain, it is reasonable to use the stratiform fraction as representative of MCS activity and as depleting parameter. However, our study showed that strictly stratiform rain shows only weak to moderate depletion rates, which is why the use of the stratiform fraction for the rate of depletion might be misleading. Moreover, deep and shallow convection with their opposing $\delta^{18}O_P$ effects are classified into the same category within the classical definition of the stratiform fraction. This leads to ambiguity in using the stratiform fraction for the interpretation of stable isotopes.

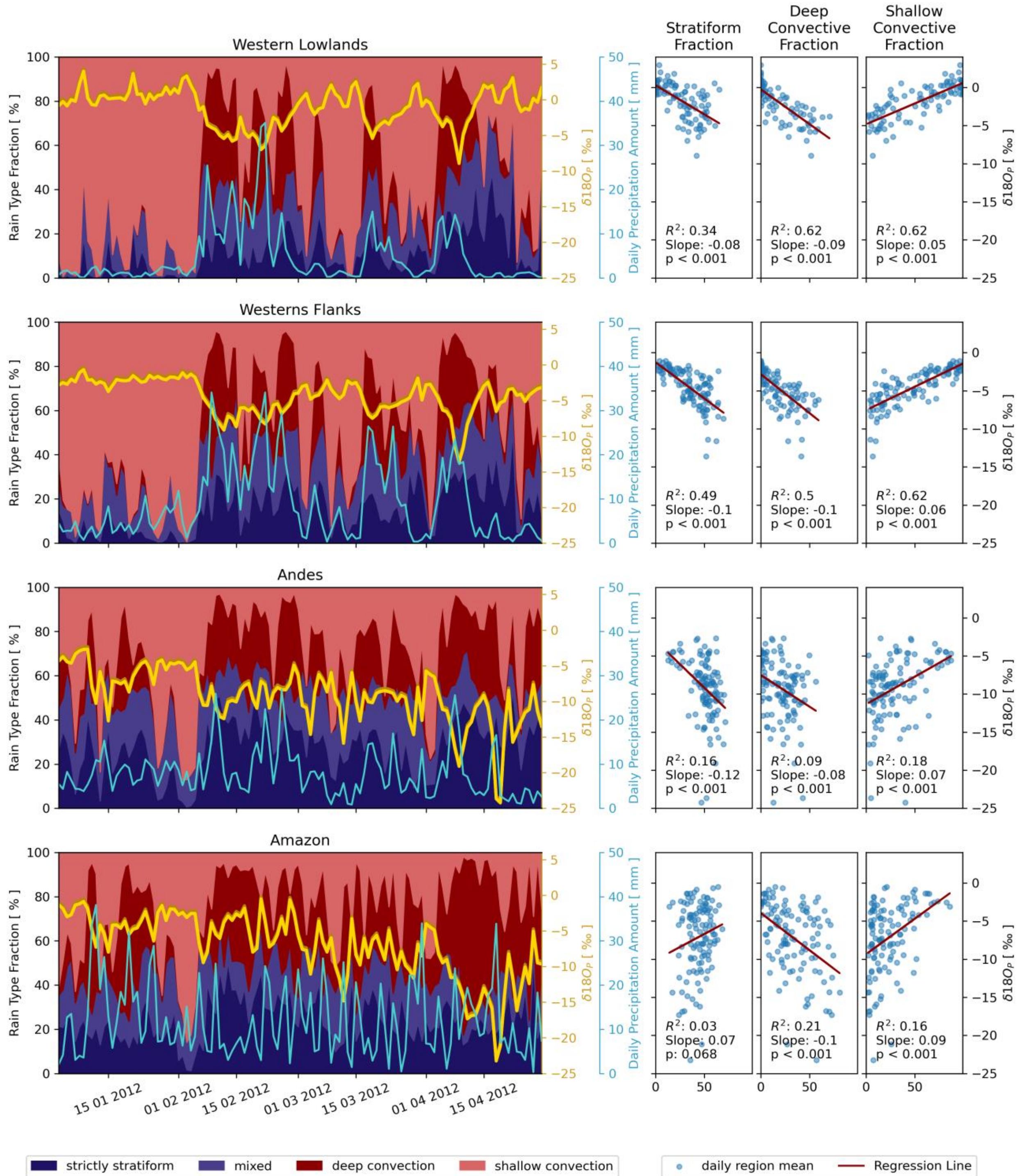

Figure 12. Time series of proportions of rain types (first column) for the different regions (rows) with daily mean $\delta^{18}O_P$ (yellow with darkyellow shadow) and the daily rain sums (cyan). Regression and the respective scatter plot between daily $\delta^{18}O_P$ and the stratiform fraction, deep convective fraction, and shallow convective fraction (second, third and last column, respectively).

3.4 Introduction of the Deep Convective Fraction and the Shallow Convective Fraction

The differing strengths in $\delta^{18}O_P$ depletion for the rain types demands a reconsideration of the stratiform fraction. As the fraction of deep convection seems to have the greatest influence on the $\delta^{18}O_P$ signal we suggest the use of a

$$deep\ convective\ fraction = \frac{\mathrm{P_{deep}}}{\mathrm{P_{all}}}$$

with daily rain sums for deep convective rain over a particular region ($\mathrm{P_{deep}}$) and all daily rain sums over the same region ($\mathrm{P_{all}}$). Deep convection occurs beside strictly stratiform and mixed rain in MSCs. All three rain types comprise snow and/or ice, which does not always allow a clear separation when using different techniques. In contrast, shallow convection is easily distinguishable due to its predominantly liquid content and it shows the least depletion rate. Therefore, we alternatively suggest a shallow convective fraction

$$shallow\ convective\ fraction = \frac{\mathrm{P_{shallow}}}{\mathrm{P_{all}}}$$

with daily rain sums for shallow convective rain over a particular region ($\mathrm{P_{shallow}}$).

Using these two definitions for the correlation with $\delta^{18}O_P$ yields an increased R^2 in contrast to the stratiform fraction (Figure 12). This particularly applies for the western lowlands, where the R^2 rises from 0.34 for the stratiform fraction to 0.62 for the deep and shallow convective fraction. The western flanks and the Andes do yield moderate improvements, and one slight decrease in the strength of the correlation (deep convective fraction for the Andes). In general, the R^2 for the Amazon and Andes is small in comparison to the western regions, which is probably linked to the high frequency of rain events with a similar composite of rain types. In contrast, the western regions, where shallow convection events clearly differ from highly depleting MCS events, reveal a more robust correlation. The most important change correlating one of the two newly defined fractions with $\delta^{18}O_P$ reveals a consistent regression sign for each region, so for west and east of the climate divide. Consequently, the dipole pattern that emerges when using the stratiform fraction (Figure 5) disappears. The deep convective fraction is consistently negatively correlated to the $\delta^{18}O_P$, whereas the shallow convective fraction exhibits a relatively positive sign. Hence, the deep or the shallow convective fraction are insensitive to a prevailing maritime or continental climate. This suggests a more robust and physically based approach representing the relation between $\delta^{18}O_P$ and rain type.

4 Conclusions

In our modeling approach with the isotope-enabled and convection-permitting $\mathrm{COSMO_{iso}}$ model, we documented and analyzed the opposing sign of the correlation between stratiform fraction and $\delta^{18}O_P$ for west (negative) and east (positive) of the Andean climate divide. The differing strengths of depletion for stratiform, shallow and deep convective rains and their relative contributions to local precipitation are in this respect of particular importance.

Shallow convection and strictly stratiform precipitation yielded the most enriched $\delta^{18}O_P$, whereas deep convection leads to the most depleted $\delta^{18}O_P$ followed by mixed rain. Shallow convection is of particular importance for total rain west of the climate divide, whereas deep convection mostly contributes to precipitation east of the climate divide. By definition, a stratiform fraction of 0 % means 100 % convective rain. The latter has usually not been separated into shallow and deep convection in past research. As these two subclasses are associated with differing $\delta^{18}O_P$ signals, the sign of correlation between stratiform fraction and $\delta^{18}O_P$ is determined by the prevailing type of convection within a region and consequently leads to opposing correlation signs. Therefore, using the stratiform fraction in stable isotope analysis might lead to ambiguous results. The application of the stratiform fraction has its justification, since tropical stratiform rain usually occurs together with deep convection like in MCS. However, we want to underline that it is the deep convection that is responsible for most of the depletion and not the stratiform rain. Consequently, we suggest, based on our derived $\delta^{18}O_P$ dependence on rain type, to use the physically more consistent deep convective fraction or shallow convective fraction for stable isotope analysis (see Section 3.4). Both metrics take into account that deep convection leads to most of the depletion, whereas on the other side, shallow convection and stratiform rain exhibit smaller depletion rates or even enrichment.

In summary our main results are

- Different rain types (stratiform, shallow and deep convective rain) are associated with distinct $\delta^{18}O_P$ and deuterium excess signals
- Deep convection leads to the strongest $\delta^{18}O_P$ depletion rate and the highest d-excess.
- It is advantageous to utilize a deep convective fraction or shallow convective fraction for correlations with $\delta^{18}O_P$.

The study results are limited by the small number of stable isotopic measurements available for evaluating the model output. Moreover, $COSMO_{iso}$ comprises a one-moment microphysics scheme that does only account for two ice species (snow and ice, not graupel and hail). However, it is to be expected that graupel and hail amounts are small in higher order microphysics schemes, which can be seen for example in the vertical distribution of hydrometeors in the study of Mölg and Kaser (2011) for a tropical, equatorial high mountain in Africa.

Our results might be of particular interest for, and applicable to paleoclimate studies. The identification of different rain types could help to interpret seasonally resolved climate proxies like stable isotopes of tree ring cellulose in Ecuador, with respect to convective activity. Questions that remain for future studies to be considered are for instance as follows:

- Do seasonally resolved climate proxies conserve the isotope signature from the occurrence of different rain types?
- How does the distribution of rain types change in the course of a year and even longer time scales?
- Is the relationship between $\delta^{18}O_P$ and deep convective fraction or shallow convective fraction consistent all over the tropics?

To answer these questions in subsequent studies, we plan to extend the model simulations to multiple years. Moreover, in an upcoming study, we want to compare these model results with seasonally resolved stable isotope measurements of collected tree ring material.

Acknowledgments

This study was funded by the Friedrich-Alexander-Universität Erlangen-Nürnberg. The authors gratefully acknowledge the scientific support and the supply of resources provided by the High Performance Computing

Center (NHR@FAU) of the Friedrich-Alexander-Universität Erlangen-Nürnberg (FAU) under the NHR project b128dc / ATMOS ("Numerical atmospheric modelling for the attribution of climate change and for model improvement"). NHR funding is provided by federal and Bavarian state authorities. NHR@FAU hardware is partially funded by the German Research Foundation (DFG) – 440719683. We acknowledge the provision of the AWS data that benefited from the financial support granted by the German Science Foundation (DFG project code BR1895/29-1) within research unit 2730 RESPECT, Martin Werner for providing the ECHAM6-wiso data; and Hans-Jürgen Panitz for his effort finding a suitable model setup for our study region.

Open Research

The MODIS AQUA and TERRA data can be accessed via http://dx.doi.org/10.5067/MODIS/MYD05_L2.006 and http://dx.doi.org/10.5067/MODIS/MOD05_L2.006, respectively (Gao, 2015). The GNIP dataset can be accessed through https://www.iaea.org/services/networks/gnip (IAEA/WMO, 2023). ECHAM6-wiso data has been described in detail in (Cauquoin & Werner, 2021) and can be accessed through https://doi.org/10.5281/zenodo.5636328 or by contacting one of the authors of this study. All details to the COSMOiso model can found in Pfahl et al. (2012). Processed data and simulation output, the Python code for reproducing the figures and the automatic weather station data can be accessed via https://doi.org/10.5281/zenodo.10438579 (Landshuter et al., 2023).

References

Aemisegger, F., Pfahl, S., Sodemann, H., Lehner, I., Seneviratne, S. I., & Wernli, H. (2014). Deuterium excess as a proxy for continental moisture recycling and plant transpiration. *Atmospheric Chemistry and Physics*, *14*(8), 4029-4054. https://doi.org/10.5194/acp-14-4029-2014

Aemisegger, F., Spiegel, J. K., Pfahl, S., Sodemann, H., Eugster, W., & Wernli, H. (2015). Isotope meteorology of cold front passages: A case study combining observations and modeling. *Geophysical Research Letters*, *42*(13), 5652-5660. https://doi.org/10.1002/2015gl063988

Aggarwal, P. K., Romatschke, U., Araguas-Araguas, L., Belachew, D., Longstaffe, F. J., Berg, P., Schumacher, C., & Funk, A. (2016). Proportions of convective and stratiform precipitation revealed in water isotope ratios. *Nature Geoscience*, *9*(8), 624-629. https://doi.org/10.1038/Ngeo2739

Allen, R. G., Pereira, L. S., Raes, D., & Smith, R. (1998). *Crop evapotranspiration - Guidelines for computing crop water requirements* (Vol. 56). FAO - Food and Agriculture Organization of the United Nations.

Ampuero, A., Stríkis, N. M., Apaéstegui, J., Vuille, M., Novello, V. F., Espinoza, J. C., Cruz, F. W., Vonhof, H., Mayta, V. C., Martins, V. T. S., Cordeiro, R. C., Azevedo, V., & Sifeddine, A. (2020). The Forest Effects on the Isotopic Composition of Rainfall in the Northwestern Amazon Basin. *Journal of Geophysical Research-Atmospheres*, *125*(4). https://doi.org/10.1029/2019JD031445

Asensio, H., Messmer, M., Lüthi, D., Osterried, K., & Jucker, J. (2020). *External Parameters for Numerical Weather Prediction and Climate Application EXTPAR. User and Implementation Guide*.

Baldauf, M., Seifert, A., Forstner, J., Majewski, D., Raschendorfer, M., & Reinhardt, T. (2011). Operational Convective-Scale Numerical Weather Prediction with the COSMO Model: Description and Sensitivities. *Monthly weather review*, *139*(12), 3887-3905. https://doi.org/10.1175/Mwr-D-10-05013.1

Ban, N., Schmidli, J., & Schär, C. (2014). Evaluation of the convection-resolving regional climate modeling approach in decade-long simulations. *Journal of Geophysical Research-Atmospheres*, *119*(13). https://doi.org/10.1002/2014jd021478

Bendix, J., Gaemmerler, S., & Reudenbach, C. (2003). A case study on rainfall dynamics during El Niño/La Niña 1997/99 in Ecuador and surrounding areas as inferred from GOES-8 and TRMM-PR observations. *Erdkunde*, *57*(2), 81-93. https://doi.org/10.3112/erdkunde.2003.02.01

Bendix, J., & Lauer, W. (1992). Die Niederschlagsjahreszeiten in Ecuador und ihre klimadynamische Interpretation. *Erdkunde*, *46*, 118-134. https://doi.org/10.3112/erdkunde.1992.02.04

Bendix, J., Trachte, K., Cermak, J., Rollenbeck, R., & Nauss, T. (2009). {Formation of Convective Clouds at the Foothills of the Tropical Eastern Andes (South Ecuador)}. *Journal of Applied Meteorology and Climatology*, *48*(8), 1682-1695. https://doi.org/10.1175/2009jamc2078.1

Bony, S., Risi, C., & Vimeux, F. (2008). Influence of convective processes on the isotopic composition (delta O-18 and delta D) of precipitation and water vapor in the tropics: 1. Radiative-convective equilibrium and Tropical Ocean-Global Atmosphere-Coupled Ocean-Atmosphere Response Experiment (TOGA-COARE) simulations. *Journal of Geophysical Research-Atmospheres*, *113*(D19). https://doi.org/10.1029/2008jd009942

Breil, M., Christner, E., Cauquoin, A., Werner, M., & Schädler, G. (2020). The dependency of the δ18O discrepancy between ice cores and model simulations on the spatial model resolution. *Climate of the Past*, *Preprint*.

Campozano, L., Trachte, K., Celleri, R., Samaniego, E., Bendix, J., Albuja, C., & Mejia, J. F. (2018). Climatology and Teleconnections of Mesoscale Convective Systems in an Andean Basin in Southern Ecuador: The Case of the Paute Basin. *Advances in Meteorology*. https://doi.org/10.1155/2018/4259191

Capotondi, A., Wittenberg, A., Newman, M., Lorenzo, E. D., Yu, J. Y., Braconnot, P., Cole, J., Dewitte, B., Giese, B., Guilyardi, E., Jin, F. F., Karnauskas, K. B., Kirtman, B., Lee, T., Schneider, N., Xue, Y., & Yeh, S. W. (2015). Understanding ENSO diversity. *Bulletin of the American Meteorological Society*, *96*(6), 921-938. https://doi.org/10.1175/BAMS-D-13-00117.1

Cauquoin, A., & Werner, M. (2021). High-Resolution Nudged Isotope Modeling With ECHAM6-Wiso: Impacts of Updated Model Physics and ERA5 Reanalysis Data. *Journal of Advances in Modeling Earth Systems*, *13*(11). https://doi.org/10.1029/2021MS002532

Chimborazo, O., & Vuille, M. (2021). Present-day climate and projected future temperature and precipitation changes in Ecuador. *Theoretical and Applied Climatology*, *143*(3-4), 1581-1597. https://doi.org/10.1007/s00704-020-03483-y

Christner, E., Aemisegger, F., Pfahl, S., Werner, M., Cauquoin, A., Schneider, M., Hase, F., Barthlott, S., & Schadler, G. (2018). The Climatological Impacts of Continental Surface Evaporation, Rainout, and Subcloud Processes on D of Water Vapor and Precipitation in Europe. *Journal of Geophysical Research-Atmospheres*, *123*(8), 4390-4409. https://doi.org/10.1002/2017jd027260

Ciais, P., & Jouzel, J. (1994). Deuterium and Oxygen-18 in Precipitation - Isotopic Model, Including Mixed Cloud Processes. *Journal of Geophysical Research-Atmospheres*, *99*(D8), 16793-16803. https://doi.org/10.1029/94jd00412

Collier, E., Sauter, T., Mölg, T., & Hardy, D. (2019). The Influence of Tropical Cyclones on Circulation, Moisture Transport, and Snow Accumulation at Kilimanjaro During the 2006-2007 Season. *Journal of Geophysical Research-Atmospheres*, *124*(13), 6919-6928. https://doi.org/10.1029/2019jd030682

Dansgaard, W. (1964). Stable isotopes in precipitation. *Tellus*, *16*, 436-468. https://doi.org/10.3402/tellusa.v16i4.8993

de Vries, A. J., Aemisegger, F., Pfahl, S., & Wernli, H. (2022). Stable water isotope signals in tropical ice clouds in the West African monsoon simulated with a regional convection-permitting model. *Atmospheric Chemistry and Physics*, *22*(13), 8863-8895. https://doi.org/10.5194/acp-22-8863-2022

Dee, S., Bailey, A., Conroy, J. L., Atwood, A., Stevenson, S., Nusbaumer, J., & Noone, D. (2023). Water isotopes, climate variability, and the hydrological cycle: recent advances and new frontiers. *Environmental Research: Climate*, *2* (022002). https://doi.org/10.1088/2752-5295/accbe1

Doms, G., Förstner, J., Heise, E., Herzog, H.-J., Mironov, D., Raschendorfer, M., Reinhardt, T., Ritter, B., Schrodin, R., Schulz, J.-P., & Vogel, G. (2011). *A Description of the Nonhydrostatic Regional COSMO Model. Part II: Physical Parameterization*. Deutscher Wetterdienst.

Emck, P. (2008). *A Climatology of South Ecuador: With Special Focus on the Major Andean Climate Divide*. VDM Verlag.

Feng, Z., Leung, L. R., Liu, N. N., Wang, J. Y., Houze, R. A., Li, J. F., Hardin, J. C., Chen, D. D., & Guo, J. P. (2021). A Global High-Resolution Mesoscale Convective System Database Using Satellite-Derived Cloud Tops, Surface Precipitation, and Tracking. *Journal of Geophysical Research-Atmospheres*, *126*(8). https://doi.org/ARTN e2020JD034202
10.1029/2020JD034202

Fosser, G., Khodayar, S., & Berg, P. (2015). Benefit of convection permitting climate model simulations in the representation of convective precipitation. *Climate Dynamics*, *44*(1-2), 45-60. https://doi.org/10.1007/s00382-014-2242-1

Fröhlich, K., Gibson, J., & Aggarwal, P. K. (2002). *Deuterium excess in precipitation and its climatological significance* Proceedings of the study of environmental change using isotope techniques, Vienna (Austria).

Fröhlich, K., Kralik, M., Papesch, W., Rank, D., Scheifinger, H., & Stichler, W. (2008). Deuterium excess in precipitation of Alpine regions - moisture recycling. *Isotopes in Environmental and Health Studies*, *44*(1), 61-70. https://doi.org/10.1080/10256010801887208

Funk, A., Schumacher, C., & Awaka, J. (2013). Analysis of Rain Classifications over the Tropics by Version 7 of the TRMM PR 2A23 Algorithm. *Journal of the Meteorological Society of Japan*, *91*(3), 257-272. https://doi.org/10.2151/jmsj.2013-302

Gao, B. (2015). *MODIS Atmosphere L2 Water Vapor Product. NASA MODIS Adaptive Processing System, Goddard Space Flight Center* https://doi.org/10.5067/MODIS/MOD05_L2.006

Gao, J., Masson-Delmotte, V., Risi, C., He, Y., & Yao, T. (2013). What controls precipitation delta O-18 in the southern Tibetan Plateau at seasonal and intra-seasonal scales? A case study at Lhasa and Nyalam. *Tellus Series B-Chemical and Physical Meteorology*, *65*. https://doi.org/10.3402/tellusb.v65i0.21043

Garcia, M., Villalba, F., Araguas-Araguas, L., & Rozanski, K. (1998). The role of atmospheric circulation patterns in controlling the regional distribution of stable isotope contents in precipitation: Preliminary results from two transects in the Ecuadorian Andes. In *Isotope Techniques in the Study of Environmental Change* (pp. 127-140). International Atomic Energy Agency.

Gat, J. R. (1996). Oxygen and hydrogen isotopes in the hydrologic cycle. *Annual Review of Earth and Planetary Sciences*, *24*, 225-262. https://doi.org/10.1146/annurev.earth.24.1.225

Gonfiantini, R., Roche, M. A., Olivry, J. C., Fontes, J. C., & Zuppi, G. M. (2001). The altitude effect on the isotopic composition of tropical rains. *Chemical Geology*, *181*(1-4), 147-167. https://doi.org/10.1016/S0009-2541(01)00279-0

Graf, P., Wernli, H., Pfahl, S., & Sodemann, H. (2019). A new interpretative framework for below-cloud effects on stable water isotopes in vapour and rain. *Atmospheric Chemistry and Physics*, *19*(2), 747-765. https://doi.org/10.5194/acp-19-747-2019

Hoffmann, G., Ramirez, E., Taupin, J. D., Francou, B., Ribstein, P., Delmas, R., Durr, H., Gallaire, R., Simoes, J., Schotterer, U., Stievenard, M., & Werner, M. (2003). Coherent isotope history of Andean ice cores over the last century. *Geophysical Research Letters*, *30*(4). https://doi.org/10.1029/2002gl014870

Houze, R. A. (2004). Mesoscale convective systems. *Reviews of Geophysics*, *42*(4). https://doi.org/10.1029/2004rg000150

Houze, R. A. (2014). *Cloud Dynamics* (2nd ed., Vol. International Geophysics). Elsevier.

Houze, R. A., Rasmussen, K. L., Zuluaga, M. D., & Brodzik, S. R. (2015). The variable nature of convection in the tropics and subtropics: A legacy of 16years of the Tropical Rainfall Measuring Mission satellite. *Reviews of Geophysics*, *53*(3), 994-1021. https://doi.org/10.1002/2015rg000488

Hu, J., Emile-Geay, J., Nusbaumer, J., & Noone, D. (2018). Impact of Convective Activity on Precipitation delta O-18 in Isotope-Enabled General Circulation Models. *Journal of Geophysical Research-Atmospheres*, *123*(23), 13595-13610. https://doi.org/10.1029/2018jd029187

IAEA/WMO. (2023). *Global Network of Isotopes in Precipitation (GNIP)* https://www.iaea.org/services/networks/gnip

Johnson, R. H., Rickenbach, T. M., Rutledge, S. A., Ciesielski, P. E., & Schubert, W. H. (1999). Trimodal characteristics of tropical convection. *Journal of Climate*, *12*(8), 2397-2418. https://doi.org/10.1175/1520-0442(1999)012%3C2397:TCOTC%3E2.0.CO;2

Klingaman, N. P., Martin, G. M., & Moise, A. (2017). ASoP (v1.0): a set of methods for analyzing scales of precipitation in general circulation models. *Geoscientific Model Development*, *10*(1), 57-83. https://doi.org/10.5194/gmd-10-57-2017

Korolev, A., McFarquhar, G., Field, P. R., Franklin, C., Lawson, P., Wang, Z., Williams, E., Abel, S. J., Axisa, D., Borrmann, S., Crosier, J., Fugal, J., Krämer, M., Lohmann, U., Schlenczek, O., Schnaiter, M., & Wendisch, M. (2017). Mixed-Phase Clouds: Progress and Challenges. *Meteorological Monographs*, *58*, 5.1-5.50. https://doi.org/10.1175/AMSMONOGRAPHS-D-17-0001.1

Kropač, E., Mölg, T., Cullen, N. J., Collier, E., Pickler, C., & Turton, J. V. (2021). A Detailed, Multi-Scale Assessment of an Atmospheric River Event and Its Impact on Extreme Glacier Melt in the Southern Alps of New Zealand. *Journal of Geophysical Research-Atmospheres*, *126*(9). https://doi.org/10.1029/2020JD034217

Kurita, N. (2013). Water isotopic variability in response to mesoscale convective system over the tropical ocean. *Journal of Geophysical Research-Atmospheres*, *118*(18), 10376-10390. https://doi.org/10.1002/jgrd.50754

Kurita, N., Noone, D., Risi, C., Schmidt, G. A., Yamada, H., & Yoneyama, K. (2011). Intraseasonal isotopic variation associated with the Madden-Julian Oscillation. *Journal of Geophysical Research-Atmospheres*, *116*. https://doi.org/10.1029/2010jd015209

Lacour, J. L., Risi, C., Worden, J., Clerbaux, C., & Coheur, P. F. (2018). Importance of depth and intensity of convection on the isotopic composition of water vapor as seen from IASI and TES delta D observations. *Earth and Planetary Science Letters*, *481*, 387-394. https://doi.org/10.1016/j.epsl.2017.10.048

Landshuter, N., Aemisegger, F., & Mölg, T. (2023). *Data and Code: Stable water isotope signals and their relation to stratiform and convective precipitation in the tropical Andes.* Zenodo. https://doi.org/10.5281/zenodo.10438579

Landshuter, N., Mölg, T., Grießinger, J., Bräuning, A., & Peters, T. (2020). 10-year Characteristics of Moisture Source Regions and Their Potential Effect on Seasonal Isotopic Signatures of delta O-18 in Tropical Trees of Southern Ecuador. *Frontiers in Earth Science*, *8*. https://doi.org/10.3389/feart.2020.604804

Lee, J. E., & Fung, I. (2008). "Amount effect" of water isotopes and quantitative analysis of post-condensation processes. *Hydrological Processes*, *22*(1), 1-8. https://doi.org/10.1002/hyp.6637

Lee, K. O., Aemisegger, F., Pfahl, S., Flamant, C., Lacour, J. L., & Chaboureau, J. P. (2019). Contrasting stable water isotope signals from convective and large-scale precipitation phases of a heavy precipitation event in southern Italy during HyMeX IOP 13: a modelling perspective. *Atmospheric Chemistry and Physics*, *19*(11), 7487-7506. https://doi.org/10.5194/acp-19-7487-2019

Lekshmy, P. R., Midhun, M., Ramesh, R., & Jani, R. A. (2014). O-18 depletion in monsoon rain relates to large scale organized convection rather than the amount of rainfall. *Scientific Reports*, *4*. https://doi.org/10.1038/srep05661

Liu, X. D., Osher, S., & Chan, T. (1994). Weighted Essentially Nonoscillatory Schemes. *Journal of Computational Physics*, *115*(1), 200-212. https://doi.org/10.1006/jcph.1994.1187

Marshall, J., & Plumb, R. A. (2008). *Atmosphere, Ocean and Climate Dynamics. An Introductory Text.* (R. Dmowska, D. Hartmann, & T. Rossby, Eds. Vol. 93). Elsevier.

McCarroll, D., & Loader, N. J. (2004). Stable isotopes in tree rings. *Quaternary Science Reviews*, *23*(7-8), 771-801. https://doi.org/10.1016/j.quascirev.2003.06.017

McPhaden, M. J., Zebiak, S. E., & Glantz, M. H. (2006). ENSO as an integrating concept in Earth science. *Science*, *314*(5806), 1740-1745. https://doi.org/10.1126/science.1132588

Mellor, G. L., & Yamada, T. (1974). Hierarchy of Turbulence Closure Models for Planetary Boundary-Layers. *Journal of the Atmospheric Sciences*, *31*(7), 1791-1806. https://doi.org/10.1175/1520-0469(1974)031%3C1791:AHOTCM%3E2.0.CO;2

Merlivat, L., & Jouzel, J. (1979). Global Climatic Interpretation of the Deuterium-Oxygen-18 Relationship for Precipitation. *Journal of Geophysical Research-Oceans*, *84*(Nc8), 5029-5033. https://doi.org/10.1029/JC084iC08p05029

Mölders, N., & Kramm, G. (2014). *Lectures in Meteorology*. Springer. https://doi.org/10.1007/978-3-319-02144-7

Mölg, T., Grosshauser, M., Hemp, A., Hofer, M., & Marzeion, B. (2012). Limited forcing of glacier loss through land-cover change on Kilimanjaro. *Nature Climate Change*, *2*(4), 254-258. https://doi.org/10.1038/Nclimate1390

Mölg, T., & Kaser, G. (2011). A new approach to resolving climate-cryosphere relations: Downscaling climate dynamics to glacier-scale mass and energy balance without statistical scale linking. *Journal of Geophysical Research-Atmospheres*, *116*. https://doi.org/10.1029/2011jd015669

Moore, M., Kuang, Z., & Blossey, P. N. (2014). A moisture budget perspective of the amount effect. *Geophysical Research Letters*, *41*(4), 1329-1335. https://doi.org/10.1002/2013gl058302

Munksgaard, N. C., Kurita, N., Sanchez-Murillo, R., Ahmed, N., Araguas, L., Balachew, D. L., Bird, M. I., Chakraborty, S., Chinh, N. K., Cobb, K. M., Ellis, S. A., Esquivel-Hernandez, G., Ganyaglo, S. Y., Gao, J., Gastmans, D., Kaseke, K. F., Kebede, S., Morales, M. R., Mueller, M., . . . Zwart, C. (2019). Data Descriptor: Daily observations of stable isotope ratios of rainfall in the tropics. *Scientific Reports*, *9*. https://doi.org/10.1038/s41598-019-50973-9

Natali, S., Doveri, M., Giannecchini, R., Baneschi, I., & Zanchetta, G. (2022). Is the deuterium excess in precipitation a reliable tracer of moisture sources and water resources fate in the western Mediterranean? New insights from Apuan Alps (Italy). *Journal of Hydrology*, *614*. https://doi.org/10.1016/j.jhydrol.2022.128497

Panitz, H. J., Dosio, A., Buchner, M., Luthi, D., & Keuler, K. (2014). COSMO-CLM (CCLM) climate simulations over CORDEX-Africa domain: analysis of the ERA-Interim driven simulations at 0.44A degrees and 0.22A degrees resolution. *Climate Dynamics*, *42*(11-12), 3015-3038. https://doi.org/10.1007/s00382-013-1834-5

Pfahl, S., & Sodemann, H. (2014). What controls deuterium excess in global precipitation? *Climate of the Past*, *10*, 771–781. https://doi.org/10.5194/cp-10-771-2014

Pfahl, S., Wernli, H., & Yoshimura, K. (2012). The isotopic composition of precipitation from a winter storm - a case study with the limited-area model COSMOiso. *Atmospheric Chemistry and Physics*, *12*(3), 1629-1648. https://doi.org/10.5194/acp-12-1629-2012

Prein, A. F., Ge, M., Valle, A. R., Wang, D., & Giangrande, S. E. (2022). Towards a Unified Setup to Simulate Mid-Latitude and Tropical Mesoscale Convective Systems at Kilometer-Scales. *Earth and Space Science*, *9*(8). https://doi.org/10.1029/2022EA002295

Pucha-Cofrep, D., Peters, T., & Bräuning, A. (2015). Wet season precipitation during the past century reconstructed from tree-rings of a tropical dry forest in Southern Ecuador. *Global and Planetary Change*, *133*, 65-78. https://doi.org/10.1016/j.gloplacha.2015.08.003

Risi, C., Bony, S., & Vimeux, F. (2008). Influence of convective processes on the isotopic composition (delta O-18 and delta D) of precipitation and water vapor in the tropics: 2. Physical interpretation of the amount effect. *Journal of Geophysical Research-Atmospheres*, *113*(D19). https://doi.org/10.1029/2008jd009943

Risi, C., Muller, C., & Blossey, P. (2020). What Controls the Water Vapor Isotopic Composition Near the Surface of Tropical Oceans? Results From an Analytical Model Constrained by Large-Eddy Simulations. *Journal of Advances in Modeling Earth Systems*, *12*(8). https://doi.org/10.1029/2020MS002106

Ritter, B., & Geleyn, J. F. (1992). A Comprehensive Radiation Scheme for Numerical Weather Prediction Models with Potential Applications in Climate Simulations. *Monthly weather review*, *120*(2), 303-325. https://doi.org/10.1175/1520-0493(1992)120%3C0303:ACRSFN%3E2.0.CO;2

Rollenbeck, R., & Bendix, J. (2011). Rainfall distribution in the Andes of southern Ecuador derived from blending weather radar data and meteorological field observations. *Atmospheric Research*, *99*(2), 277-289. https://doi.org/10.1016/j.atmosres.2010.10.018

Samuels-Crow, K. E., Galewsky, J., Sharp, Z. D., & Dennis, K. J. (2014). Deuterium excess in subtropical free troposphere water vapor: Continuous measurements from the Chajnantor Plateau, northern Chile. *Geophysical Research Letters*, *41*(23), 8652-8659. https://doi.org/10.1002/2014GL062302

Schättler, U., Doms, G., & Schraff, C. (2013). *A Description of the Nonhydrostatic Regional COSMO-Model. Part VII. User's Guide* (U. Schättler, Ed.). Deutscher Wetterdienst Business Area "Research and Development".

Schumacher, C., & Houze, R. A. (2003). Stratiform rain in the tropics as seen by the TRMM precipitation radar. *Journal of Climate*, *16*(11), 1739-1756. https://doi.org/10.1175/1520-0442(2003)016%3C1739:SRITTA%3E2.0.CO;2

Spannl, S., Volland, F., Pucha, D., Peters, T., Cueva, E., & Bräuning, A. (2016). Climate variability, tree increment patterns and ENSO-related carbon sequestration reduction of the tropical dry forest species Loxopterygium huasango of Southern Ecuador. *Trees-Structure and Function*, *30*(4), 1245-1258. https://doi.org/10.1007/s00468-016-1362-0

Steppeler, J., Doms, G., Schättler, U., Bitzer, H. W., Gassmann, A., Damrath, U., & Gregoric, G. (2003). Meso-gamma scale forecasts using the nonhydrostatic model LM. *Meteorology and Atmospheric Physics*, *82*(1-4), 75-96. https://doi.org/10.1007/s00703-001-0592-9

Su, J. Z., Xiang, B. Q., Wang, B., & Li, T. (2014). Abrupt termination of the 2012 Pacific warming and its implication on ENSO prediction. *Geophysical Research Letters*, *41*(24), 9058-9064. https://doi.org/10.1002/2014gl062380

Sui, C. H., Tsay, C. T., & Li, X. F. (2007). Convective - stratiform rainfall separation by cloud content. *Journal of Geophysical Research-Atmospheres*, *112*(D14). https://doi.org/10.1029/2006jd008082

Temme, F., Turton, J. V., Mölg, T., & Sauter, T. (2020). Flow Regimes and Fohn Types Characterize the Local Climate of Southern Patagonia. *Atmosphere*, *11*(9). https://doi.org/10.3390/atmos11090899

Tharammal, T., Bala, G., & Noone, D. (2017). Impact of deep convection on the isotopic amount effect in tropical precipitation. *Journal of Geophysical Research-Atmospheres*, *122*(3), 1505-1523. https://doi.org/10.1002/2016jd025555

Thompson, L. G., Mosley-Thompson, E., & Henderson, K. A. (2000). Ice-core palaeoclimate records in tropical South America since the Last Glacial Maximum. *Journal of Quaternary Science*, *15*(4), 377-394. https://doi.org/10.1002/1099-1417(200005)15:4%3C377::AID-JQS542%3E3.0.CO;2-L

Thurnherr, I., Hartmuth, K., Jansing, L., Gehring, J., Boettcher, M., Gorodetskaya, I., Werner, M., Wernli, H., & Aemisegger, F. (2021). The role of air–sea fluxes for the water vapour isotope signals in the cold and warm sectors of extratropical cyclones over the Southern Ocean. *Weather Clim. Dynam.*, *2*(2), 331-357. https://doi.org/10.5194/wcd-2-331-2021

Tiedtke, M. (1989). A Comprehensive Mass Flux Scheme for Cumulus Parameterization in Large-Scale Models. *Monthly weather review*, *117*(8), 1779-1800. https://doi.org/10.1175/1520-0493(1989)117%3C1779:ACMFSF%3E2.0.CO;2

Trachte, K. (2018). Atmospheric Moisture Pathways to the Highlands of the Tropical Andes: Analyzing the Effects of Spectral Nudging on Different Driving Fields for Regional Climate Modeling. *Atmosphere*, *9*(11). https://doi.org/10.3390/atmos9110456

Vargas, D., Chimborazo, O., Laszlo, E., Temovski, M., & Palcsu, L. (2022). Rainwater Isotopic Composition in the Ecuadorian Andes and Amazon Reflects Cross-Equatorial Flow Seasonality. *Water*, *14*(13). https://doi.org/10.3390/w14132121

Vergara-Temprado, J., Ban, N., Panosetti, D., Schlemmer, L., & Schar, C. (2020). Climate Models Permit Convection at Much Coarser Resolutions Than Previously Considered. *Journal of Climate*, *33*(5), 1915-1933. https://doi.org/10.1175/Jcli-D-19-0286.1

Victoria, R. L., Martinelli, L. A., Mortatti, J., & Richey, J. (1991). Mechanisms of Water Recycling in the Amazon Basin - Isotopic Insights. *Ambio*, *20*(8), 384-387. (https://www.jstor.org/stable/4313869)

Villiger, L., Dütsch, M., Bony, S., Lothon, M., Pfahl, S., Wernli, H., Brilouet, P.-E., Chazette, P., Coutris, P., Delanoë, J., Flamant, C., Schwarzenboeck, A., Werner, M., & Aemisegger, F. (2023). Water isotopic characterisation of the cloud-circulation coupling in the North Atlantic trades. Part 1: A process-oriented evaluation of COSMOiso simulations with EUREC4A observations. *EGUsphere [preprint]*. https://doi.org/10.5194/egusphere-2023-449

Vimeux, F., Gallaire, R., Bony, S., Hoffmann, G., & Chiang, J. C. H. (2005). What are the climate controls on delta D in precipitation in the Zongo Valley (Bolivia)? Implications for the Illimani ice core interpretation. *Earth and Planetary Science Letters*, *240*(2), 205-220. https://doi.org/10.1016/j.epsl.2005.09.031

Volland-Voigt, F., Bräuning, A., Ganzhi, O., Peters, T., & Maza, H. (2011). Radial stem variations of Tabebuia chrysantha (Bignoniaceae) in different tropical forest ecosystems of southern Ecuador. *Trees-Structure and Function*, *25*(1), 39-48. https://doi.org/10.1007/s00468-010-0461-6

Wang, B. (1994). Climatic Regimes of Tropical Convection and Rainfall. *Journal of Climate*, *7*(7), 1109-1118. https://doi.org/10.1175/1520-0442(1994)007%3C1109:CROTCA%3E2.0.CO;2

Wang, B., & Xu, X. H. (1997). Northern hemisphere summer monsoon singularities and climatological intraseasonal oscillation. *Journal of Climate*, *10*(5), 1071-1085. https://doi.org/10.1175/1520-0442(1997)010%3C1071:NHSMSA%3E2.0.CO;2

Wilks, D. S. (2011). *Statistical Methods in the Atmospheric Sciences* (R. Dmowska, D. Hartmann, & H. T. Rossby, Eds. Vol. 100). Academic Press.

Zhiña, D. X., Mosquera, G. M., Esquivel-Hernández, G., Córdova, M., Sánchez-Murillo, R., Orellana-Alvear, J., & Crespo, P. (2022). Hydrometeorological Factors Controlling the Stable Isotopic Composition of Precipitation in the Highlands of South Ecuador. *Journal of Hydrometeorology*, *23*(7), 1059-1074. https://doi.org/10.1175/Jhm-D-21-0180.1

Zwart, C., Munksgaard, N. C., Kurita, N., & Bird, M. I. (2016). Stable isotopic signature of Australian monsoon controlled by regional convection. *Quaternary Science Reviews*, *151*, 228-235. https://doi.org/10.1016/j.quascirev.2016.09.010

Journal of Geophysical Research: Atmospheres

Supporting Information for

Stable water isotope signals and their relation to stratiform and convective precipitation in the tropical Andes

Nadja Landshuter[1], Franziska Aemisegger[2] and Thomas Mölg[1]

[1]Climate System Research Group, Institute of Geography, Friedrich-Alexander-Universität Erlangen-Nürnberg, Erlangen, Germany.
[2]Institute for Atmospheric and Climate Science, ETH Zurich, Zurich, Switzerland

Contents of this file

Figures S1 to S7

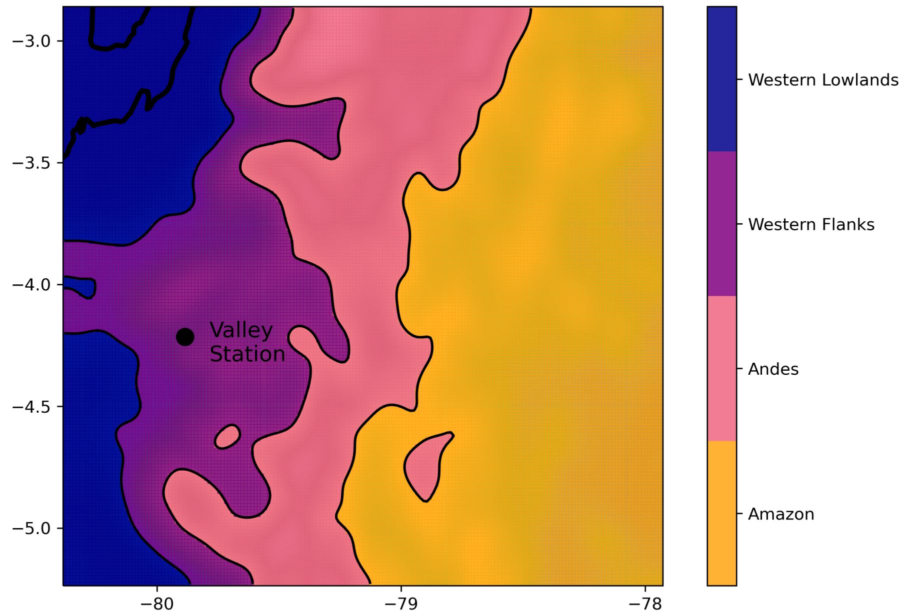

Figure S1. Spatial extent of the four regions defined in Data & Methods (see Study Site) and as used in Figure 11.

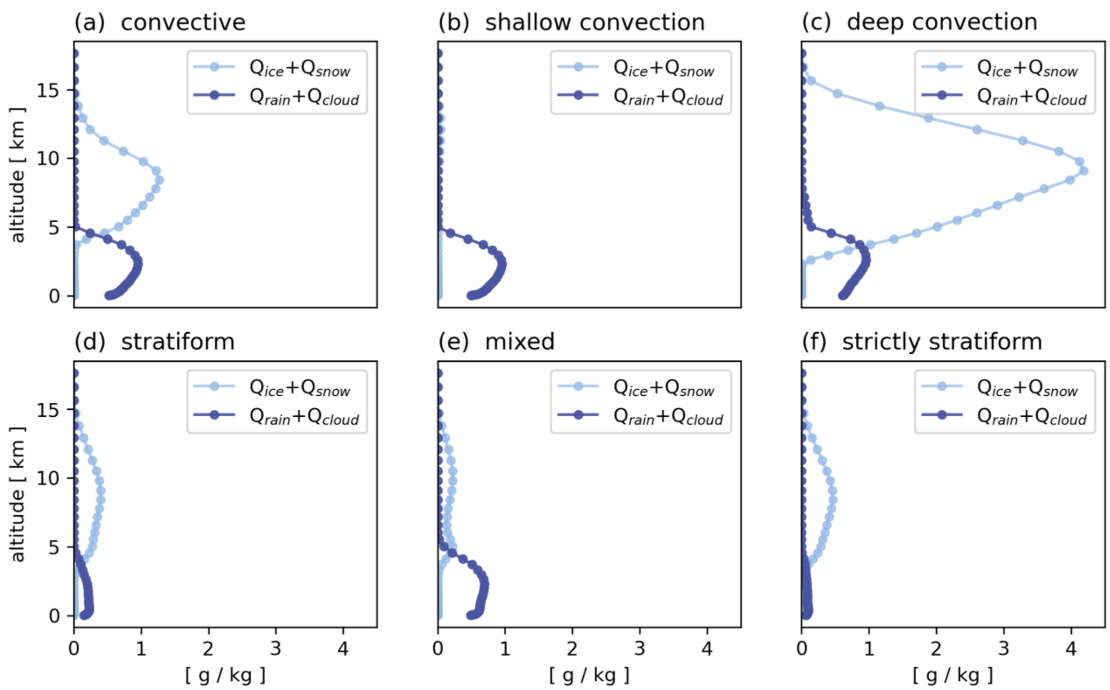

Figure S2. Vertical distribution of the 90th percentile of the frozen hydrometeors (Q_{ice} + Q_{snow}) and the liquid ones (Q_{rain} +Q_{cloud}) for convective and stratiform rain ((a) and (d), respectively) and their subclasses shallow convection, deep convection, mixed and strictly stratiform ((b), (c), (e) and (f), respectively) covering the period from January 2012 to April 2012.

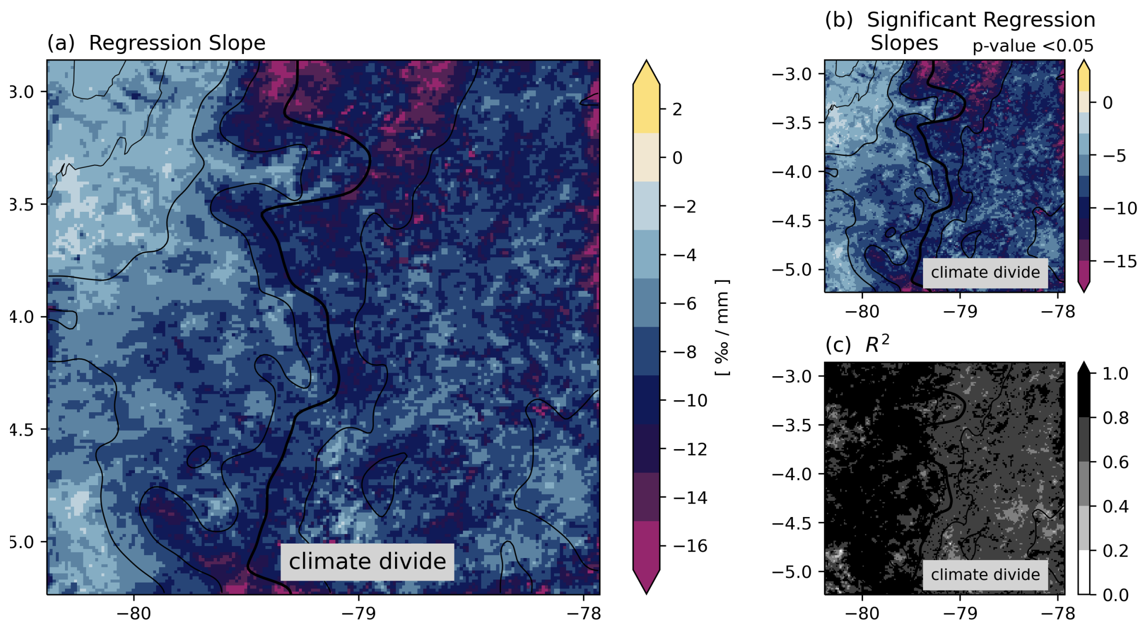

Figure S3. Regression slope between $\delta^{18}O_P$ and daily mean rain rates (amount effect) (a), significant regression slopes with *p*-values < 0.05 and additionally accounting for field significance by minimizing the false discovery rate (b) and R^2 of the correlation (c).

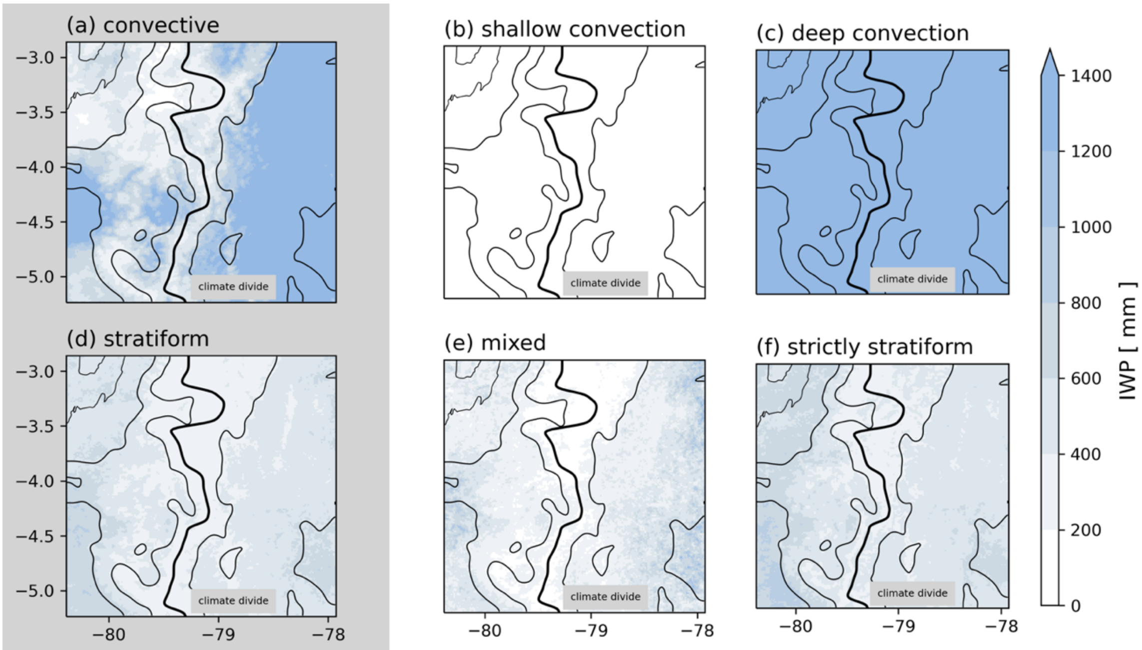

Figure S4. As Figure 8, but for the ice water path (IWP).

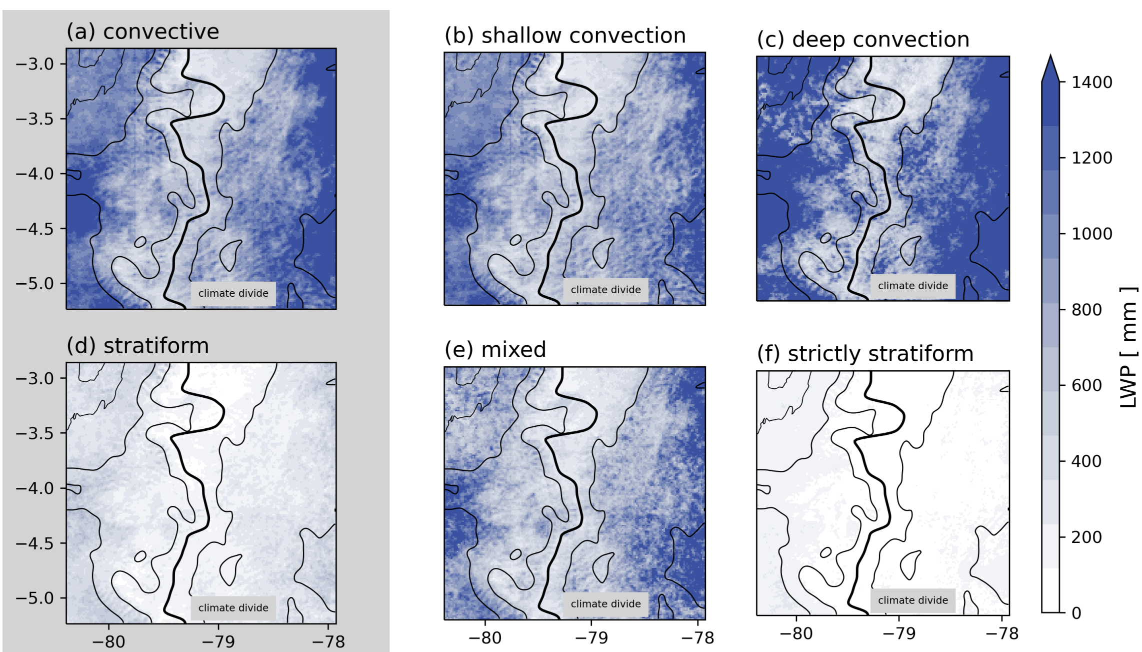

Figure S5. As Figure 8, but for the liquid water path (LWP).

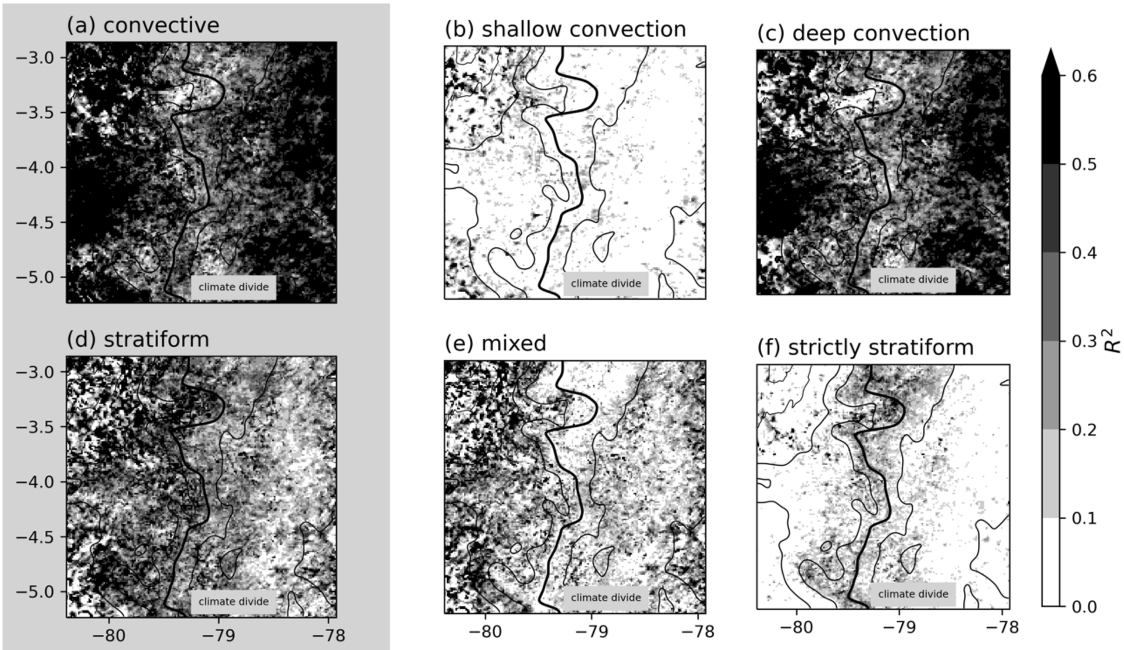

Figure S6. R^2 of amount effect for each rain type.

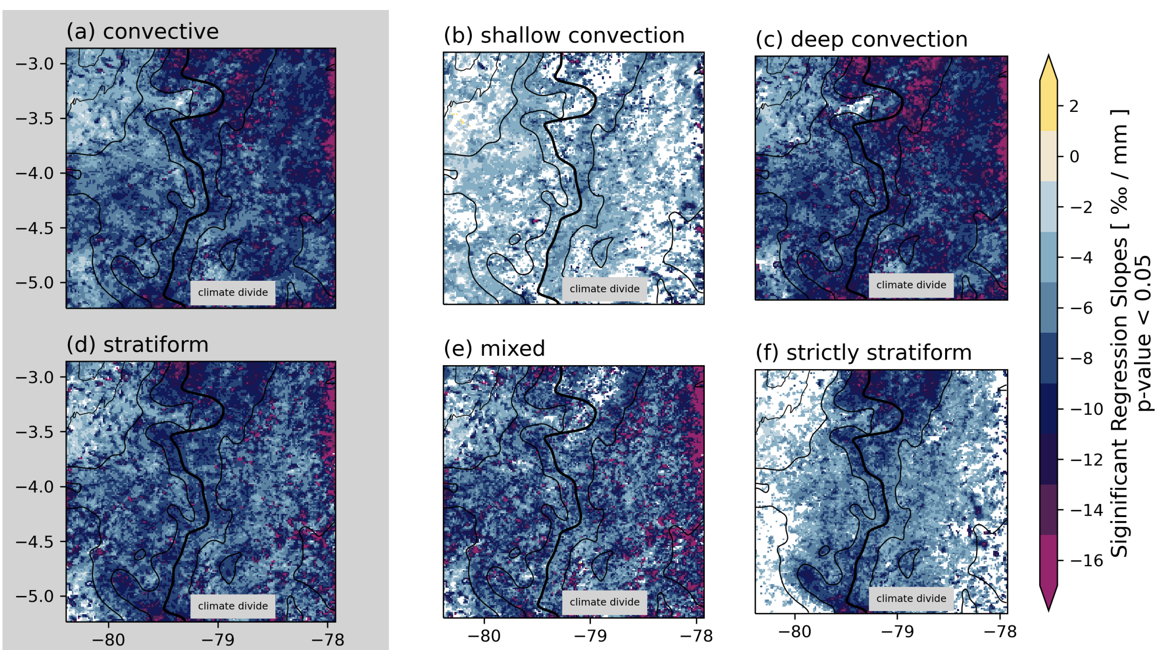

Figure S7. Significant regression slopes of the amount effect for each rain type (*p*-value < 0.05 and additionally accounting for field significance by minimizing the false discovery rate).